HUNTINGTON DISEASE

Development of a ligand for in vivo imaging of mutant huntingtin in Huntington's disease

Daniele Bertoglio[1]*†, Jonathan Bard[2]†, Manuela Hessmann[3], Longbin Liu[2], Annette Gärtner[3], Stef De Lombaerde[1,4], Britta Huscher[3], Franziska Zajicek[1], Alan Miranda[1], Finn Peters[3], Frank Herrmann[3], Sabine Schaertl[3], Tamara Vasilkovska[5], Christopher J. Brown[6], Peter D. Johnson[6], Michael E. Prime[6], Matthew R. Mills[6], Annemie Van der Linden[5], Ladislav Mrzljak[2], Vinod Khetarpal[2], Yuchuan Wang[2], Deanna M. Marchionini[2], Mette Skinbjerg[2], Jeroen Verhaeghe[1], Celia Dominguez[2], Steven Staelens[1]*, Ignacio Munoz-Sanjuan[2]*

Huntington's disease (HD) is a dominantly inherited neurodegenerative disorder caused by a CAG trinucleotide expansion in the huntingtin (*HTT*) gene that encodes the pathologic mutant HTT (mHTT) protein with an expanded polyglutamine (polyQ) tract. Whereas several therapeutic programs targeting mHTT expression have advanced to clinical evaluation, methods to visualize mHTT protein species in the living brain are lacking. Here, we demonstrate the development and characterization of a positron emission tomography (PET) imaging radioligand with high affinity and selectivity for mHTT aggregates. This small molecule radiolabeled with ^{11}C ([^{11}C]CHDI-180R) allowed noninvasive monitoring of mHTT pathology in the brain and could track region- and time-dependent suppression of mHTT in response to therapeutic interventions targeting mHTT expression in a rodent model. We further showed that in these animals, therapeutic agents that lowered mHTT in the striatum had a functional restorative effect that could be measured by preservation of striatal imaging markers, enabling a translational path to assess the functional effect of mHTT lowering.

INTRODUCTION

Neurodegenerative disease pathology is characterized by the presence of insoluble protein deposits in different subcellular compartments, which mark alterations in cellular homeostasis. Typically, neurodegenerative disorders have a complex molecular etiology, and affected brain cells display aggregation of a variety of proteins. In Huntington's disease (HD), a CAG tract expansion beyond 39 repeats in exon 1 of the huntingtin (*HTT*) gene is sufficient to cause the disease in a fully penetrant manner (*1*). HD can be considered a multisystem atrophy disorder, although the main pathological findings show ample degeneration of spiny projection neurons (SPNs) in the caudate and putamen, neurons in the globus pallidus and subthalamic nucleus of the basal ganglia, as well as substantial but variable degeneration in neurons of the cerebral cortex and thalamic, cerebellar, and hypothalamic nuclei (*2*). Mutant huntingtin (mHTT) protein deposition in the neuropil and nucleus has variable morphology, is more frequent in some classes of projection neurons than in interneurons, and is less frequent in cells of glial origin. A well-described progression "map" of degeneration pathology and aggregate deposition has been available for some time, although it is not clear how well histopathological changes inform the clinical staging of HD (*2*, *3*).

A longstanding goal for HD has been to target the cause of the disease. Therapeutic programs targeting HTT expression have advanced to clinical stages, including a now-terminated open-label extension study and phase 3 trial that were evaluating the sustained safety and efficacy of tominersen, an antisense oligonucleotide (ASO) delivered intrathecally that can lower both mutant and wild-type (wt) HTT (www.clinicaltrials.gov, identifiers NCT03842969, NCT03761849, and NCT03342053). (*4*, *5*) The first gene therapy vector-mediated phase 1/2 trial is now underway testing AMT-130, an adeno-associated virus (AAV) AAV5–microRNA (miRNA) targeting both *HTT* alleles delivered directly into the caudate and putamen of HD patients (*6*) (www.clinicaltrials.gov, identifier NCT04120493). Delivery of both of these agents is invasive and characterized by a restricted distribution that varies because of the modalities used: The ASO predominantly decreases HTT expression in the spinal cord, cortical areas, and cerebellum, with some drugs reaching deeper basal ganglia nuclei, whereas the AAV-miRNA targets mostly the striatum and associated connected cell bodies via axonal transport (*6*, *7*). Although the distribution and pharmacological activity of these therapeutics have been extensively evaluated in nonhuman primates and mHTT-expressing transgenic minipigs (*7*), it is unclear whether we can expect a similar distribution in the larger human brain.

A key milestone was reached when the Ionis/Roche phase 1/2a trial (*4*) (www.clinicaltrials.gov, identifier NCT02519036) showed for the first time sustained dose- and time-dependent decreases in cerebrospinal fluid (CSF) concentration of mHTT, demonstrating pharmacological activity in the human central nervous system (CNS). Regrettably, this finding has not led to clinical benefit in the recently terminated phase 3 tominersen trial, and analyses are underway to understand the safety issues identified, which led to a worsening of disease symptoms in the cohort treated once every 8 weeks. How the reduction of mHTT in CSF after delivery of ASOs via lumbar puncture and AAVs delivered into brain parenchyma (*5*, *7*) relates to lowering in affected circuits in the brain remains unclear.

To evaluate regional pharmacological effects of candidate therapeutics targeting mHTT, we sought to develop a noninvasive imaging agent specific for aggregated mHTT that could give insight into

[1]Molecular Imaging Center Antwerp (MICA), University of Antwerp, Wilrijk 2610, Belgium. [2]CHDI Management/CHDI Foundation, Los Angeles, CA 90045, USA. [3]Evotec SE, Hamburg 22419, Germany. [4]Department of Nuclear Medicine, Antwerp University Hospital, Edegem 2650, Belgium. [5]Bio-Imaging Lab, University of Antwerp, Wilrijk 2610, Belgium. [6]Evotec Ltd., Abingdon OX14 4RZ, UK.
*Corresponding author. Email: daniele.bertoglio@uantwerpoen.be (D.B.); steven.staelens@uantwerpen.be (S. Staelens); ignacio.munoz@chdifoundation.org (I.M.-S.)
†These authors contributed equally to this work.

the timing, durability, and regional therapeutic effects of administered drugs (*8*–*10*). As all current therapeutic agents in development (*11*) target either *HTT* or HTT transcriptional or posttranscriptional processes, quantification of mHTT protein could offer a good indicator of the extent of HTT lowering and of the biodistribution of the agents. [^{11}C]CHDI-180R was identified and developed into a positron emission tomography (PET) tracer through a medicinal chemistry campaign from an initial small-molecule screen that yielded mHTT aggregate binders (*8*–*10*). CHDI-180 is a high-affinity (1 to 3 nM), cell-permeable ligand, specific for mHTT aggregates and unable to bind unexpanded HTT, monomeric soluble mHTT, or nuclear inclusion bodies. We have demonstrated binding to mHTT-derived fibrils generated from recombinant protein, and mHTT aggregates expressed in mouse HD models and human HD samples, whose precise state(s) (for example, oligomer or protofibril) has yet to be defined.

Here, we investigate the utility of a PET imaging ligand with high affinity and selectivity for mHTT aggregation to detect mHTT aggregation in affected brain cells and its application as indicator of pharmacological activity of agents that target HTT expression in the living brain. Specifically, we describe the ability of [^{11}C]CHDI-180R to identify time-, dose-, and region-specific pharmacological effects in two distinct interventional paradigms: direct striatal delivery of AAVs expressing zinc finger protein (ZFP) repressors selectively targeting mHTT (*12*) in the zQ175 HD mouse model (*13*, *14*), and in a genetically regulatable Q140 knock-in (KI) HD mouse model, the LacQ140^{l}(*), that enables ~50% systemic lowering of m*Htt* mRNA and mHTT protein in a time-controlled manner. We further explore whether imaging agents for striatal markers with diminished expression in HD [specifically phosphodiesterase 10a (PDE10a) and dopamine receptors] (*8*, *15*–*19*) can detect the protective effects of mHTT lowering interventions in a time-dependent manner and serve as functional response indicator for mHTT lowering with translational potential.

RESULTS

CHDI-180 specifically binds mHTT in HD animal models

Aggregate pathology was detected with [^{3}H]CHDI-180 autoradiography (ARG) already at 4 weeks of age in R6/2 mice (Fig. 1, A and B). F1 In the zQ175DN heterozygous (het) model, aggregation is slower but detectable binding was measured at 6 months of age, increasing progressively until 13 months of age (Fig. 1, C and D), in a pattern that mirrors histological analysis using mEM48 detection (*20*). Because R6/2 and the zQ175DN models express large expansions in the polyglutamine (polyQ) tract, we explored the HdhQ80 KI model (*21*) expressing smaller CAG lengths to understand whether aggregate pathology could be detected with finer temporal and spatial manner. Figure 1 (E and F) shows that CHDI-180 binding follows a ventrodorsal gradient of aggregation within the striatum of HdhQ80 animals, beginning at 12 months of age in the homozygotes (hom). This pattern of aggregate pathology within the striatum was confirmed histochemically (Fig. 1, G and H) with mEM48 antibody detection.

CHDI-180 does not colocalize with nuclear inclusion bodies in HD animal models and human brains

The CHDI-180 ligand was initially identified using radioligand binding assays for expanded HTT proteins produced recombinantly (*8*). However, mHTT aggregates can have different forms and can be detected in distinct subcellular compartments (intranuclear inclusions, diffuse nuclear-aggregated species, soma-localized aggregates, or neuropil aggregates). These species of oligomerized/aggregated mHTT can be detected with antibodies against aggregated, polyQ expanded mHTT, such as mEM48 (*22*) or PHP-1 (*23*). Therefore, we conducted double co-detection studies (binding and immunostaining), using [^{3}H]CHDI-180 ARG and mEM48 immunohistochemistry (IHC) (Fig. 1, I and J, and figs. S1 and S2) in brain sections derived from zQ175DN and HdhQ80 mice and postmortem human HD carriers. CHDI-180 binding did not colocalize with intranuclear inclusions detected by mEM48 in the zQ175DN model (Fig. 1I and fig. S2, A to C) or in the HdhQ80 mouse model (Fig. 1J and fig. S1), with most signal observed outside the nucleus, presumably to neuropil or soma-localized mHTT aggregates. A similar pattern is observed in human brain samples from HD individuals (Fig. 1K and fig. S2G). There was no binding to the wt mouse brain (figs. S1, J to L, and S2, D to F) or in the brains of unaffected human subjects (fig. S2H) in either the gray or white matter under the autoradiographic conditions used.

[^{11}C]CHDI-180R PET imaging enables in vivo quantification of mHTT pathology

To examine the in vivo kinetic properties of [^{11}C]CHDI-180R (*8*) as a PET ligand, we selected the zQ175DN model because it displays a moderately slow disease onset, with hallmark of mHTT aggregates increasing from 3 to 12 months (*20*). We performed in vivo microPET studies in 9-month-old zQ175DN het and wt mice for characterization of its pharmacokinetic properties and monitored its stability in the brain and plasma (fig. S3A).

Radio–high-performance liquid chromatography (radio-HPLC) coupled with γ-counter measurement of mouse brain homogenates and plasma samples did not show [^{11}C]CHDI-180R–related metabolites in zQ175DN mice independent of genotype and mHTT inclusion amount (4- and 10-month-old het) (fig. S3, B and C). Next, to evaluate [^{11}C]CHDI-180R kinetics, we performed 90-min dynamic microPET scans after intravenous injection. We extracted an image-derived input function (IDIF) (fig. S3E) from the heart blood pool of each animal to serve as a noninvasive input function (*24*, *25*). Injection of [^{11}C]CHDI-180R (table S1) resulted in a rapid radioactive uptake in the brain with standardized uptake value (regional radioactivity normalized to the injected activity and body weight) showing genotypic difference over the 90-min period and reversible kinetics described by a two-tissue compartment model (2TCM) (fig. S3F and table S2). The resulting striatal total volume of distribution using IDIF [$V_{T\,(IDIF)}$ as a surrogate of V_T (*26*)] in het zQ175DN was significantly increased by 62% compared to wt littermates ($P < 0.0001$; fig. S3G) with extremely low coefficients of variation (wt = 2.84%, het = 5.2%; fig. S3G). Scan acquisition could be reduced from 90 min down to 60 min ($R^2 = 0.99$, $P < 0.0001$; fig. S3H), and reliable $V_{T\,(IDIF)}$ estimation of [^{11}C]CHDI-180R binding was also obtained using the Logan graphical analysis (*27*) as demonstrated by the optimal linear relationship ($y = 1.08x - 0.04$) with $V_{T\,(IDIF)}$ estimation using 2TCM ($R^2 = 0.99$, $P < 0.0001$; fig. S3I). Last, $V_{T\,(IDIF)}$ parametric maps of [^{11}C]CHDI-180R using the Logan model could be generated for both zQ175DN wt and het mice (fig. S3J).

Longitudinal characterization of [^{11}C]CHDI-180R PET ligand allows detection of temporal dynamics of mHTT pathology

We performed a longitudinal evaluation of [^{11}C]CHDI-180R microPET imaging in zQ175DN het and wt mice (Fig. 2A and table S3). In F2 zQ175DN, mHTT-containing inclusions initiate in striatum (*20*), and the striatum was the first region where significant $V_{T\,(IDIF)}$ differences

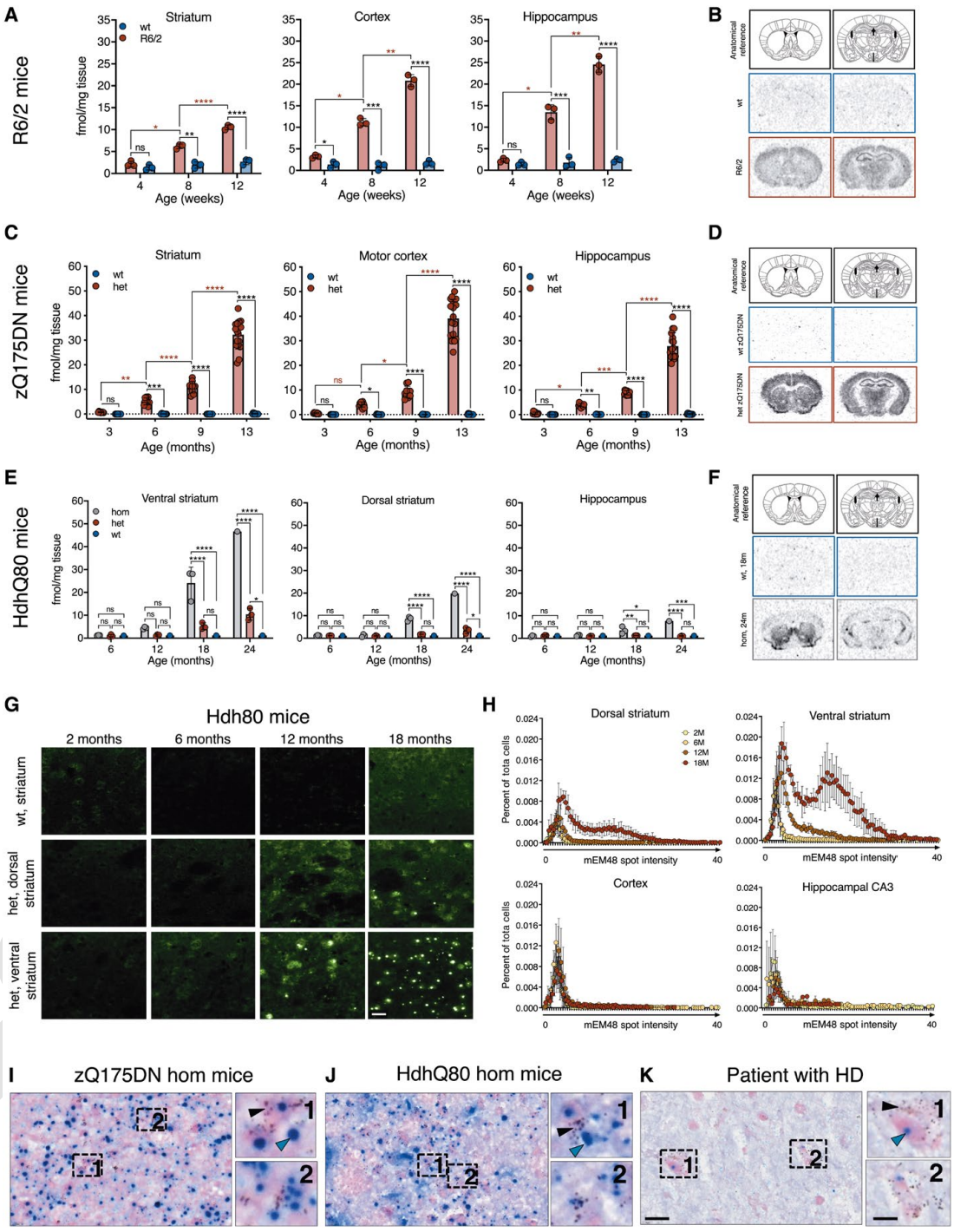

Fig. 1. [^{3}H]CHDI-180 mHTT-specific binding in HD mouse models without colocalizing with mHTT inclusions. (**A** and **B**) Binding to transgenic R6/2 CAG120 mouse brains expressing mutant human exon 1 Htt. (A) Genotype-specific age-dependent increase in [^{3}H]CHDI-180 in striatum, cortex, and hippocampus of 4-, 8-, and 12-week-old R6/2 CAG120 and wt littermates (wt, $n = 3$; R6/2, $n = 3$; per age). Two-way analysis of variance (ANOVA) with Tukey's multiple comparison test. Red asterisk denotes signal differences between ages, as indicated for R6/2 mice. One representative study out of $n > 15$ experiments shown. (B) Representative autoradiograms showing total binding of [^{3}H]CHDI-180 in the striatum, cortex, and hippocampus of 12-week-old R6/2 and wt mice; anatomical orientation as indicated. (**C** and **D**) Binding to knock-in zQ175DN het mouse brains carrying a humanized exon 1 Htt sequence with 198 CAG repeats. (C) Genotype-specific age–dependent increase in [^{3}H]CHDI-180 in striatum, cortex, and hippocampus of 3, 6, and 9 months (wt, $n = 10$; het, $n = 10$, per age) and 13 months (wt, $n = 13$; het, $n = 17$) of age. Two-way ANOVA with Tukey's multiple comparison test. Red asterisk denotes signal differences between ages, as indicated for zQ175DN het mice. (D) Representative autoradiograms showing total binding of [^{3}H]CHDI-180 in striatum, cortex, and hippocampus of 13-month-old zQ175DN het and wt mice; anatomical orientation as indicated. (**E** to **H**) Binding to knock-in HdhQ80 mouse brains carrying a humanized exon 1 Htt sequence with 86 CAG repeats. (E) Genotype-specific age-dependent increase in [^{3}H]CHDI-180 in ventral and dorsal striatum as well as hippocampus at 6, 9, 18, and 24 months (wt, $n = 1$ to 3; het, $n = 3$; hom, $n = 1$ to 3, per age) of age. Two-way ANOVA with Tukey's multiple comparison test. (F) Representative autoradiograms showing total binding of [^{3}H]CHDI-180 in striatum, cortex, and hippocampus of 24-month-old HdhQ80 hom and wt mice; anatomical orientation as indicated. (G) Representative mHTT inclusion (mEM48) immunostaining in the dorsal and ventral striatum of HdhQ80 wt and het mice indicates that [^{3}H]CHDI-180 binding is associated with the age- and brain region–dependent appearance of mEM48-positive mHTT inclusions as shown by mEM48 immunohistochemistry. Scale bar, 20 μm. (H) Quantitative analysis of mEM48 intensity in HdhQ80 mice for mHTT inclusions in different brain regions and age groups. (**I** to **K**) Colocalization of [^{3}H]CHDI-180 binding and mHTT inclusions (mEM48) in the ventral striatum of 12-month-old hom zQ175DN mice (I), ventral striatum of 24-month-old hom Hdh80 mice (J), and postmortem frontal cortex of a patient with HD (#2017-060) (K). [^{3}H]CHDI-180 silver grain signal was detectable in close vicinity to mEM48-positive signal but never coregistered with mHTT inclusion bodies, although it was partially coregistered with more diffuse-appearing mEM48-positive signal. [^{3}H]CHDI-180 binding, black silver grains, black arrowhead; mHTT inclusions (mEM48), blue, blue arrowhead; background tissue (Nuclear Fast Red), pink. Scale bar, 20 μm; inset, 10 μm. Data are shown as means ± SD; all points are shown; $^*P < 0.05$, $^{**}P < 0.01$, $^{***}P < 0.001$, and $^{****}P < 0.0001$.

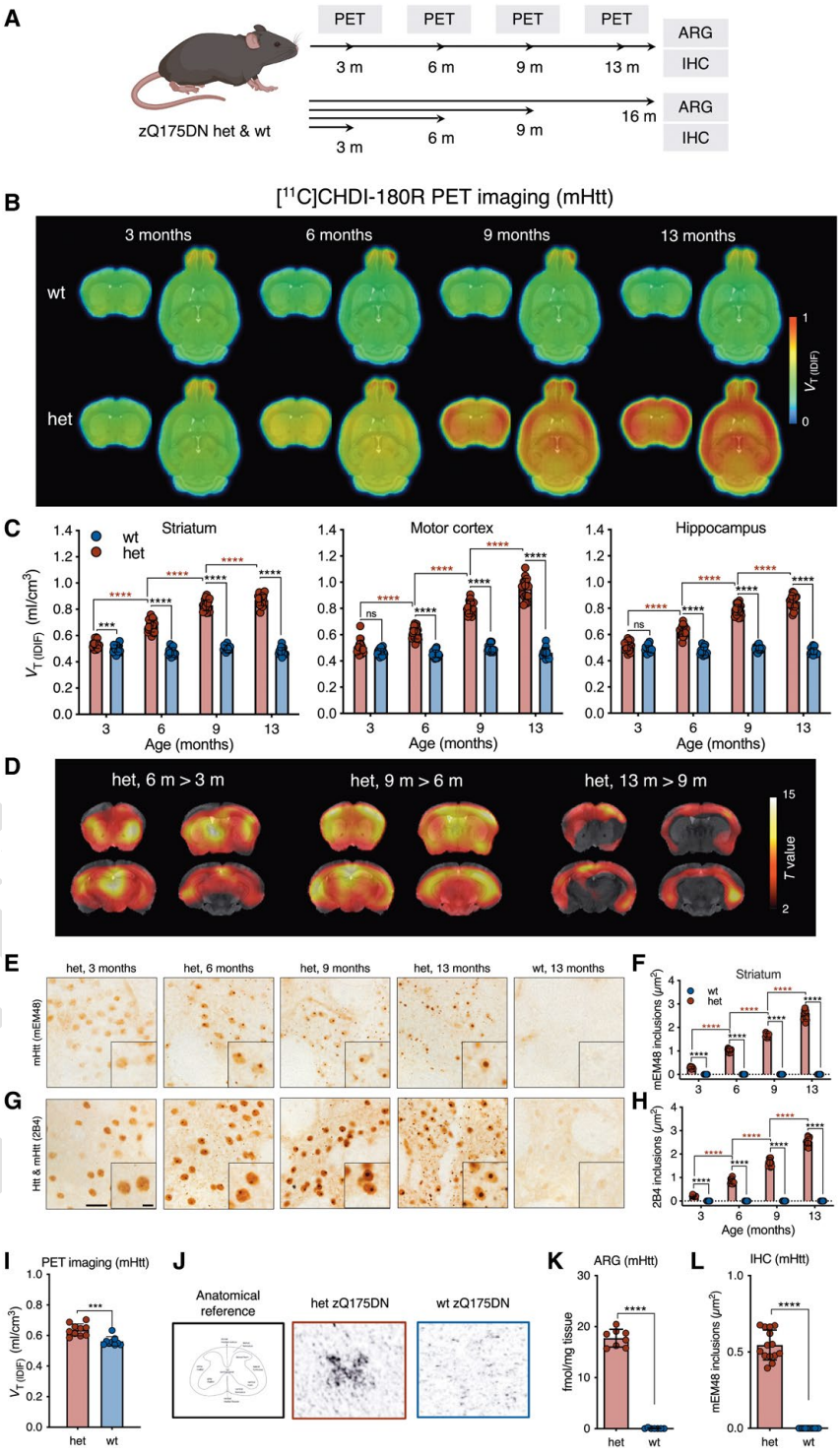

Fig. 2. Longitudinal characterization of natural disease in zQ175DN het mice using [^{11}C]CHDI-180R PET imaging. (**A**) Timeline overview and endpoints in zQ175DN wt and het mice. Upper timeline refers to the longitudinal in vivo study, whereas lower one refers to the cross-sectional postmortem studies. (**B**) Mean [^{11}C]CHDI-180R $V_{T\ (IDIF)}$ parametric images of zQ175DN wt and het mice at 3, 6, 9, and 13 months of age. PET images are coregistered to the MRI template for anatomical reference. Coronal and axial planes are shown. (**C**) Regional [^{11}C]CHDI-180R $V_{T\ (IDIF)}$ quantification in zQ175DN wt and het at 3 months (wt, $n = 19$; het, $n = 21$), 6 months (wt, $n = 15$; het, $n = 23$), 9 months (wt, $n = 13$; het, $n = 20$), and 13 months (wt, $n = 12$; het, $n = 17$) of age. Repeated measures with linear mixed model analysis with Tukey-Kramer correction; ***$P < 0.001$ and ****$P < 0.0001$. Red asterisks denote longitudinal differences within zQ175DN het mice. (**D**) Within zQ175DN het voxel-based analysis of [^{11}C]CHDI-180R $V_{T\ (IDIF)}$ parametric images. Comparison between 3 and 6 months ($n = 21$), 6 and 9 months ($n = 20$), and 9 and 13 months ($n = 17$) of age. Significant ($P < 0.001$) clusters are coregistered to the MRI template for anatomical reference and shown in the coronal panel. (**E** and **G**) Genotype-specific age-dependent accumulation of mHTT inclusions in zQ175DN het mice at time points matching the longitudinal [^{11}C]CHDI-180R PET study as demonstrated by mEM48 (E) and 2B4 (G) immunostaining. Scale bar, 20 μm; inset scale bar, 5 μm. (**F** and **H**) Quantification of inclusions in wt and zQ175DN het mice for mEM48 (F) and 2B4 (H) at 3 months (wt, $n = 10$; het, $n = 10$), 6 months (wt, $n = 10$; het, $n = 10$), 9 months (wt, $n = 10$; het, $n = 10$), and 13 months (wt, $n = 13$; het, $n = 17$) of age. Two-way ANOVA with Bonferroni's multiple comparison test. Red asterisks denote longitudinal differences within zQ175DN het mice. (**I**) Spinal cord [^{11}C]CHDI-180R $V_{T\ (IDIF)}$ quantification in zQ175DN wt and het at 13 months (wt, $n = 9$; het, $n = 10$) of age. Two-tailed unpaired t test with Welch's correction. (**J**) Representative autoradiograms showing total binding of [^{3}H]CHDI-180 in the spinal cord of zQ175DN wt and het mice at 16 months; anatomical reference as indicated. (**K**) Specific binding of [^{3}H]CHDI-180 in the spinal cord of zQ175DN wt and het mice at 16 months (wt, $n = 7$; het, $n = 8$) of age. Two-tailed unpaired t test with Welch's correction. (**L**) Quantification of spinal cord inclusions in zQ175DN wt and het mice for mEM48 at 16 months (wt, $n = 13$; het, $n = 15$) of age. Two-tailed unpaired t test with Welch's correction; ****$P < 0.0001$. ARG, autoradiography. Data are shown as means ± SD; all points shown; ***$P < 0.001$ and ****$P < 0.0001$.

were detected at 3 months of age ($P < 0.001$; Fig. 2, B and C). [^{11}C]CHDI-180R $V_{T\ (IDIF)}$ values revealed stable values over time in wt mice given the lack of specific target, whereas het zQ175DN displayed a significant temporal increase in all brain regions [striatum, 6.7% ($P < 0.001$), 40.3% ($P < 0.0001$), 63.1% ($P < 0.0001$), and 81.3% ($P < 0.0001$), at 3, 6, 9, and 13 months of age, respectively] (Fig. 2C). For sample size requirements in therapeutic studies in het zQ175DN mice, see table S4. The increasing [^{11}C]CHDI-180R binding within zQ175DN het was also confirmed by the voxel-based analysis of [^{11}C]CHDI-180R $V_{T\ (IDIF)}$ parametric maps, which could also identify specific cortical clusters of increased binding at advanced disease (13 m > 9 m; Fig. 2D).

We monitored mHTT inclusions by mEM48 and 2B4 (*28*) immunoreactivity (Fig. 2A). In line with the [^{11}C]CHDI-180R microPET findings, striatal mHTT inclusions could be observed starting at 3 months of age with a significant increase in size with disease progression in het zQ175DN mice for both mEM48 ($P < 0.0001$; Fig. 2, E and F) and 2B4 (*28*) ($P < 0.0001$; Fig. 2, G and H), whereas no mHTT inclusion was detected in wt littermates (fig. S4).

Within the CNS, mHTT inclusions are not limited to the brain as they may be found in the spinal cord in human patients (*29*). In the cervical spinal cord of zQ175DN het mice, [^{11}C]CHDI-180R binding

was significantly increased compared to wt littermates ($P < 0.001$; Fig. 2I) as also confirmed by [^{3}H]CHDI-180 ARG ($P < 0.0001$; Fig. 2, J and K) and mEM48 immunostaining ($P < 0.0001$; Fig. 2L).

[^{11}C]CHDI-180R imaging identifies time- and region-dependent changes in mHTT pathology after virally mediated, mHTT-selective striatal knockdown in the zQ175DN model

Given the ability of [^{11}C]CHDI-180R to detect the temporal evolution of the mHTT pathology in live animals, we examined its applicability in measuring the effect of local or global mHTT lowering strategies (Figs. 3A, 4A, and 5B and tables S5 to S9). We have previously demonstrated that striatal ZFP-mediated mHTT repression could improve molecular, histopathological, and electrophysiological deficits in the zQ175 het mice (*12*). In this work, we used the ZFP-D repressor driven by the human synapsin promoter (*12*) in two experimental paradigms to assess binding changes when the treatment is administered before disease onset (early treatment) compared to administration after disease symptoms are well manifested (late treatment) (Figs. 3A and 4A) (*12*–*14*). Het zQ175DN or wt mice were injected into striata with either AAV ZFP (treatment), ZFP lacking the DNA binding domain (ZFP-ΔDBD; control), or vehicle (phosphate-buffered saline) before (2 months of age) or after (5 months of age) the age of mHTT inclusion formation and disease onset (Figs. 3B and 4B) (*13*, *14*). As shown in Fig. 3B, we designed the experiment in a way that each animal acts as its own control; in one cohort, zQ175DN mice are injected with active ZFP in the left hemisphere, and with an inactive ZFP-ΔDBD in the right hemisphere. A second cohort of zQ175DN mice and a cohort of wt mice were injected with the vehicle in the left hemisphere, to control for the potential impact of viral transduction and exogenous protein expression, and with the control ZFP-ΔDBD in the right hemisphere. Animals were monitored longitudinally via [^{11}C]CHDI-180R PET. In addition, other biomarkers known to undergo early, progressive, and profound changes years before clinical diagnosis, PDE10a, D_1R, and $D_{2/3}$R (*15*, *17*, *30*–*32*), were assessed longitudinally using [^{18}F]MNI-659, [^{11}C]SCH23390, and [^{11}C]Raclopride, respectively (tables S5 and S6). In the early intervention paradigm, mHTT pathology and PDE10a were assessed in vivo. During the late intervention paradigm, one study cohort was imaged for mHTT pathology and PDE10a, whereas a second cohort was analyzed for D_1R and $D_{2/3}$R. At the study end, in vivo findings were corroborated by ARG and immunostaining. Progressive alterations in these markers are recapitulated in zQ175DN het mice (*8*, *12*, *16*, *33*–*35*).

In the early ZFP intervention (Fig. 3, A and B, and tables S5 and S8), [^{11}C]CHDI-180R $V_{T\ (IDIF)}$ values for the ZFP- versus ΔDBD-injected striatum were significantly reduced by 2.8, 9.0, and 16.3% at 3, 6, and 10 months of age, respectively (treatment effect: $P < 0.0001$; Fig. 3, C and E). No difference was observed for control zQ175DN cohorts (Fig. 3, C and E, and fig. S5, A and B). The reduced [^{11}C]CHDI-180R binding was paralleled by a significant increase in the nondisplaceable binding potential [BP_{ND}, a quantitative index of receptor density (*26*)] for [^{18}F]MNI-659 (22.7, 98.1, and 98.1% at 3, 6, and 10 months of age, respectively, treatment effect: $P < 0.0001$, or 1, 4, and 8 months after viral transduction with ZFP-mediated mHTT suppression), with no contralateral difference for the control zQ175DN cohorts (Fig. 3, D and F, and fig. S5, C and D). The estimated "therapeutic" effect for the early or late intervention was calculated according to Eq. 1 (see Materials and Methods) as the difference in het mice between ZFP-treated hemisphere and control ΔDBD-injected hemisphere. This difference was normalized to the total genotypic difference, estimated as the delta between ΔDBD-injected striatum in wt and het mice. The resulting estimate suggested about 40% mHTT lowering (42.2, 40.6, and 38.8% at 3, 6, and 10 months of age), which was positively associated with the 43.3% PDE10a preservation in the same animals ($R^2 = 0.52$, $P < 0.0001$; Fig. 3G). Upon completion of the studies, ARG was performed using [^{3}H]CHDI-180 (mHTT), [^{3}H]SCH23390 (D_1R), and [^{3}H]Raclopride ($D_{2/3}$R) and immunostaining for PDE10a. Striatal [^{3}H]CHDI-180 binding for the ZFP- versus ΔDBD-injected striatum was significantly reduced by 53.6% ($P < 0.0001$; Fig. 3, H and I), showing correlation with the in vivo [^{11}C]CHDI-180R PET measurement ($R^2 = 0.67$, $P < 0.0001$; Fig. 3J). A significant increase in ZFP- versus ΔDBD-injected striatum was measured for PDE10a immunostaining (30.7%, $F_{2,30} = 59.40$, $P < 0.0001$), D_1R with [^{3}H]SCH23390 (40.6%, $F_{2,30} = 34.98$, $P < 0.0001$), and $D_{2/3}$R with [^{3}H]Raclopride (10.9%, $F_{2,30} = 6.59$, $P < 0.01$; Fig. 3, K to M). Noteworthy, the reduction in mHTT amount was correlated with preservation of all measured striatal markers (PDE10a: $R^2 = 0.84$, $P < 0.0001$; D_1R: $R^2 = 0.79$, $P < 0.0001$; $D_{2/3}$R: $R^2 = 0.29$, $P = 0.0012$; fig. S6).

In the late ZFP intervention paradigm (Fig. 4, A and B, and tables S6 and S9), [^{11}C]CHDI-180R $V_{T\ (IDIF)}$ values for the ZFP- versus ΔDBD-injected striatum were significantly reduced by 4.3 and 10.3% at 6 and 10 months of age ($P < 0.0001$, 1 and 5 months after viral transduction), respectively, without contralateral differences for control zQ175DN cohorts (Fig. 4, C and G, and fig. S7, A and B). In addition, a significant increase in BP_{ND} for ZFP-injected compared to ΔDBD-ZFP–injected striatum was measured for all translational biomarkers, with [^{18}F]MNI-659 being increased by 20.4 and 43.6% (Fig. 4, D and H, and fig. S7, C and D), [^{11}C]SCH23390 by 7.4 and 17.4% (Fig. 4, E and I, and fig. S7, E and F), and [^{11}C]Raclopride by 8.9 and 14.1% (Fig. 4, F and J, and fig. S7, G and H) at 6 and 10 months, respectively (treatment effect: $P < 0.0001$ for all markers). However, when the percentage difference in BP_{ND} between hemisphere was corrected by the het control group, the ZFP group displayed increased binding of 19.3 and 38.7% ([^{18}F]MNI-659), of 1.7 and 9.6% ([^{11}C]SCH23390), and of 4.5 and 4.2% ([^{11}C]Raclopride) at 6 and 10 months, respectively (treatment effect: $P < 0.0001$ for all markers; Fig. 4, H to J). The estimated therapeutic effect for the late intervention (Eq. 1) indicated about 23% mHTT lowering (19.4 and 23.6% at 6 and 10 months of age, respectively), positively associated to the 25.5% PDE10a preservation ($R^2 = 0.26$, $P = 0.002$; Fig. 4K). In postmortem experiments, [^{3}H]CHDI-180 binding for the ZFP- versus ΔDBD-injected striatum was significantly reduced by 42.1% ($F_{2,73} = 116.5$, $P < 0.0001$; Fig. 4, L and M), showing agreement with [^{11}C]CHDI-180R ($R^2 = 0.56$, $P = 0.0003$; Fig. 4N). This effect was lower than the 53.6% measured during early intervention (Fig. 3I), possibly due to time of intervention (2 or 5 months of age), the duration of the treatment (8 or 5 months), or a combination of these factors. In addition, we observed a significant increase in ZFP- versus ΔDBD-injected striatum for PDE10a (12.8%, $F_{2,63} = 52.75$, $P < 0.0001$), D_1R with [^{3}H]SCH23390 (25.6%, $F_{2,66} = 37.70$, $P < 0.0001$), and $D_{2/3}$R with [^{3}H]Raclopride (6.5%, $F_{2,66} = 3.71$, $P = 0.0297$; Fig. 4, O to Q). The preservation of all measured striatal markers in the ZFP-injected hemisphere was correlated with the reduction in mHTT protein species (PDE10a: $R^2 = 0.61$, $P < 0.0001$; D_1R: $R^2 = 0.48$, $P < 0.0001$; $D_{2/3}$R: $R^2 = 0.14$, $P = 0.0016$; figs. S6 and S8).

Meso scale discovery (MSD) measurements showed that ZFP treatment did not alter wt mouse HTT concentration [detected using the combination of mouse-specific monoclonal antibody (mAb) 2133 and the D7F7 mAb] but significantly decreased the amount of

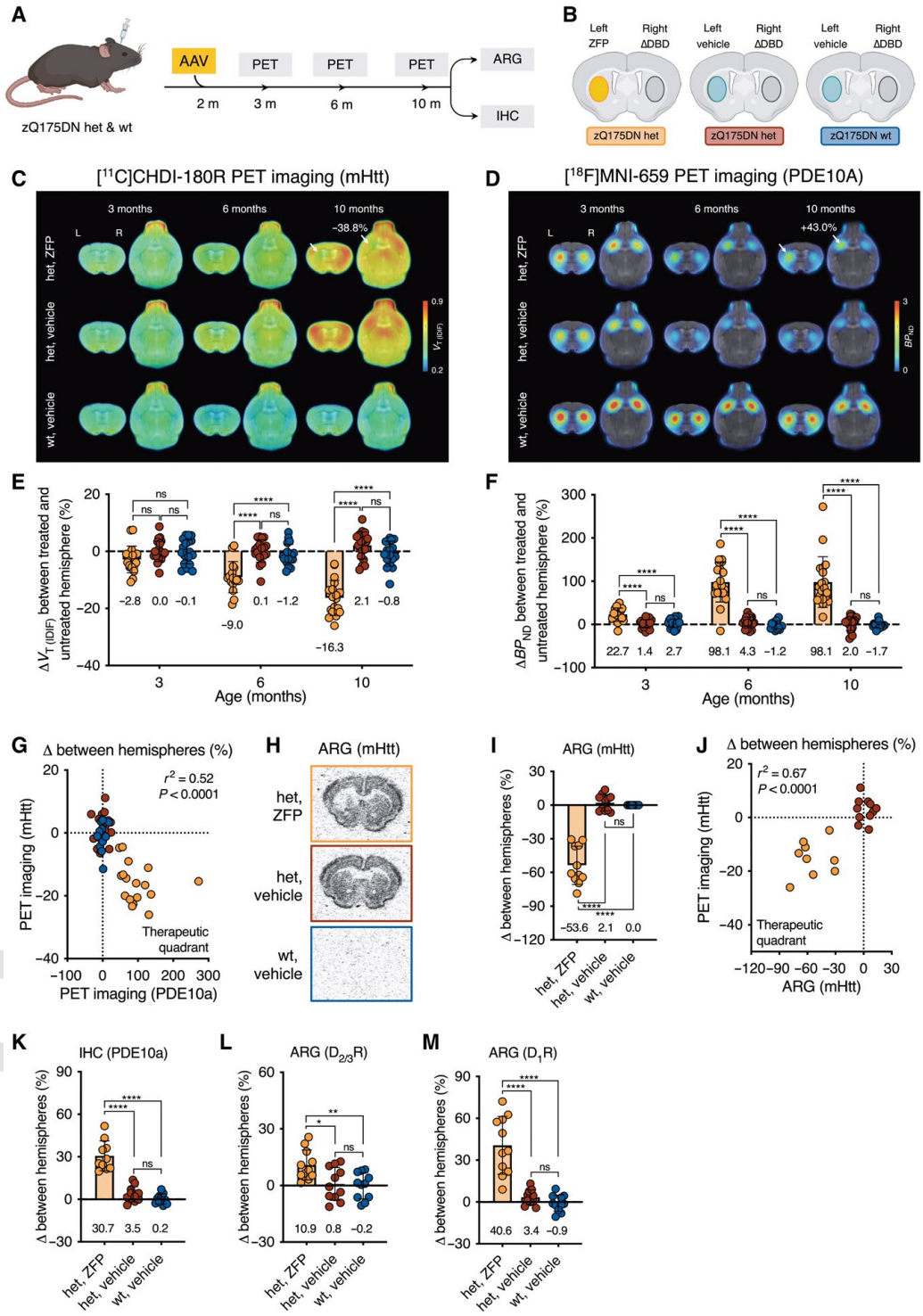

Fig. 3. Response of [^{11}C]CHDI-180R and imaging markers to early ZFP intervention in the striatum of zQ175DN mice. (**A**) Timeline overview and endpoints of early ZFP intervention in zQ175DN wt and het mice. (**B**) Experimental design overview in zQ175DN wt and het mice depicting injection hemisphere for ZFP treatment, ZFP-ΔDBD, and vehicle only. Fill colors represent the experimental group animals belong to. (**C** and **D**) Mean [^{11}C]CHDI-180R $V_{T\ (IDIF)}$ (mHTT inclusions) (C) and [^{18}F]MNI-659 BP_{ND} (PDE10a) (D) parametric images of zQ175DN wt vehicle, het vehicle, and het ZFP-treated mice at 3, 6, and 10 months of age. PET images are coregistered to the MRI template for anatomical reference. Coronal and axial planes are shown. A white arrow at 10 months of age indicates the ZFP-treated striatal hemisphere with reduced mHTT and increased PDE10a binding. (**E** and **F**) Percentage contralateral difference for striatal [^{11}C]CHDI-180R $V_{T\ (IDIF)}$ (mHTT inclusions) (E) and [^{18}F]MNI-659 BP_{ND} (PDE10a) (F) quantification in zQ175DN wt vehicle, het vehicle, and het ZFP-treated mice at 3, 6, and 10 months of age (het ZFP, $n = 18$ to 21; het vehicle, $n = 18$ to 22; wt vehicle, $n = 18$ to 20; values for each age, group, and radioligand) after striatal injection at 2 months of age. Repeated measures with linear mixed model analysis with Tukey-Kramer correction. (**G**) Correlation between contralateral difference for striatal mHTT and PDE10a binding with the het, ZFP group deviating from the center of axes toward the therapeutic quadrant. Two-tailed Pearson correlation analysis; $R^2 = 0.52$; $P < 0.0001$. (**H**) Representative autoradiograms showing total binding of [^{3}H]CHDI-180 (mHTT inclusions) in zQ175DN wt vehicle, het vehicle, and het ZFP-treated mice. (**I**) Percentage contralateral difference for striatal specific binding of [^{3}H]CHDI-180 in zQ175DN wt vehicle, het vehicle, and het ZFP-treated mice at 10 months of age (het ZFP, $n = 11$; het vehicle, $n = 11$; wt vehicle, $n = 11$) after striatal injection at 2 months of age. One-way ANOVA with Tukey's multiple comparison test. (**J**) Correlation between contralateral difference for striatal mHTT binding measured with microPET and ARG at 10 months of age depicting the het ZFP-treated mice deviating from the center of axes toward the therapeutic quadrant. Two-tailed Pearson correlation analysis; $R^2 = 0.67$; $P < 0.0001$. (**K** to **M**) Percentage contralateral difference for PDE10a immunostaining (K), [^{3}H]SCH23390 (D_1R) (L), and [^{3}H]Raclopride ($D_{2/3}$R) (M) in zQ175DN wt vehicle, het vehicle, and het ZFP-treated mice at 10 months of age (het ZFP, $n = 11$; het vehicle, $n = 11$; wt vehicle, $n = 11$) after striatal injection at 2 months of age. One-way ANOVA with Tukey's multiple comparison test. Data are shown as means ± SD; all points shown; $^*P < 0.05$, $^{**}P < 0.01$, $^{***}P < 0.001$, and $^{****}P < 0.0001$.

soluble and aggregated mHTT in both the early (39 and 69%, respectively; $P < 0.0001$; fig. S9, A to C) and late (43 and 37%, respectively; $P < 0.05$; fig. S9, D to F) intervention studies. Soluble expanded HTT protein was detected using 2B7-MW1 assay (*36*), and aggregated mHTT was detected using MW8-4C9 assay (*37*). Most likely, mHTT reduction on a level of only ZFP-expressing cells would be higher

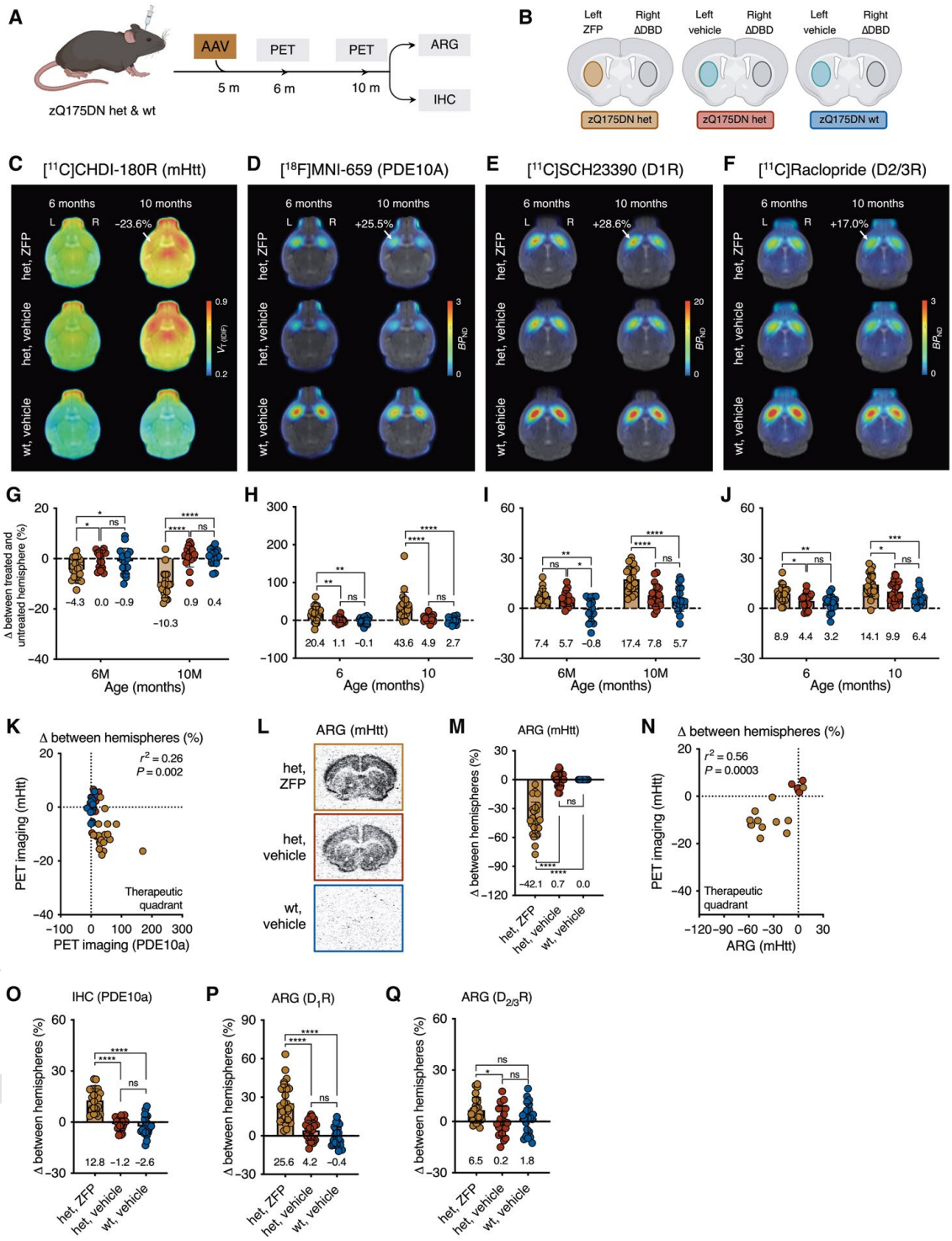

Fig. 4. Response of [^{11}C]CHDI-180R and imaging markers to late ZFP intervention in the striatum of zQ175DN mice. (**A**) Timeline overview and endpoints of late ZFP intervention in zQ175DN wt and het mice. (**B**) Experimental design overview in zQ175DN wt and het mice depicting injection hemisphere for ZFP treatment, ZFP-ΔDBD, and vehicle only. Fill colors represent the experimental group animals belong to. (**C** to **F**) Mean [^{11}C]CHDI-180R $V_{T\,(IDIF)}$ (mHTT inclusions) (C), [^{18}F]MNI-659 BP_{ND} (PDE10a) (D), [^{11}C]SCH23390 BP_{ND} (D_1R) (E), and [^{11}C]Raclopride BP_{ND} ($D_{2/3}$R) (F) parametric images of zQ175DN wt vehicle, het vehicle, and het ZFP-treated mice at 6 and 10 months of age. PET images are coregistered to the MRI template for anatomical reference. Axial plane is shown. A white arrow at 10 months of age indicates the ZFP-treated striatal hemisphere with reduced mHTT as well as increased PDE10a, D_1R, and $D_{2/3}$R binding. (**G** to **J**) Percentage contralateral difference for striatal [^{11}C]CHDI-180R $V_{T\,(IDIF)}$ (mHTT inclusions) (G), [^{18}F]MNI-659 BP_{ND} (PDE10a) (H), [^{11}C]SCH23390 BP_{ND} (D_1R) (I), and [^{11}C]Raclopride BP_{ND} ($D_{2/3}$R) (J) quantification in zQ175DN wt vehicle, het vehicle, and het ZFP-treated mice at 6 and 10 months of age (het ZFP, $n = 17$ to 23; het vehicle, $n = 16$ to 22; wt vehicle, $n = 16$ to 19; values for each age, group, and radioligand) after striatal injection at 5 months of age. Repeated measures with linear mixed model analysis with Tukey-Kramer correction. (**K**) Correlation between contralateral difference for striatal mHTT and PDE10a binding with the het, ZFP group partly deviating from the center of axes toward the therapeutic quadrant. Two-tailed Pearson correlation analysis; $R^2 = 0.26$; $P = 0.002$. (**L**) Representative autoradiograms showing total binding of [^{3}H]CHDI-180 (mHTT inclusions) in zQ175DN wt vehicle, het vehicle, and het ZFP-treated. (**M**) Percentage contralateral difference for striatal specific binding of [^{3}H]CHDI-180 in zQ175DN wt vehicle, het vehicle, and het ZFP-treated mice at 10 months of age (het ZFP, $n = 25$; het vehicle, $n = 26$; wt vehicle, $n = 25$) after striatal injection at 5 months of age. One-way ANOVA with Tukey's multiple comparison test. (**N**) Correlation between contralateral difference for striatal mHTT binding measured with microPET and ARG at 10 months of age depicting the het ZFP-treated mice partly deviating from the center of axes toward the therapeutic quadrant. Two-tailed Pearson correlation analysis; $R^2 = 0.56$; $P = 0.0003$. (**O** to **Q**) Percentage contralateral difference for immunostaining for PDE10a (O) and ARG for [^{3}H]SCH23390 (D_1R) (P) and [^{3}H]Raclopride ($D_{2/3}$R) (Q) in zQ175DN wt vehicle, het vehicle, and het ZFP-treated mice at 10 months of age (het ZFP, $n = 25$; het vehicle, $n = 26$; wt vehicle, $n = 25$) after striatal injection at 5 months of age. One-way ANOVA with Tukey's multiple comparison test. Data are shown as means ± SD; all points shown; $^*P < 0.05$, $^{**}P < 0.01$, $^{***}P < 0.001$, and $^{****}P < 0.0001$.

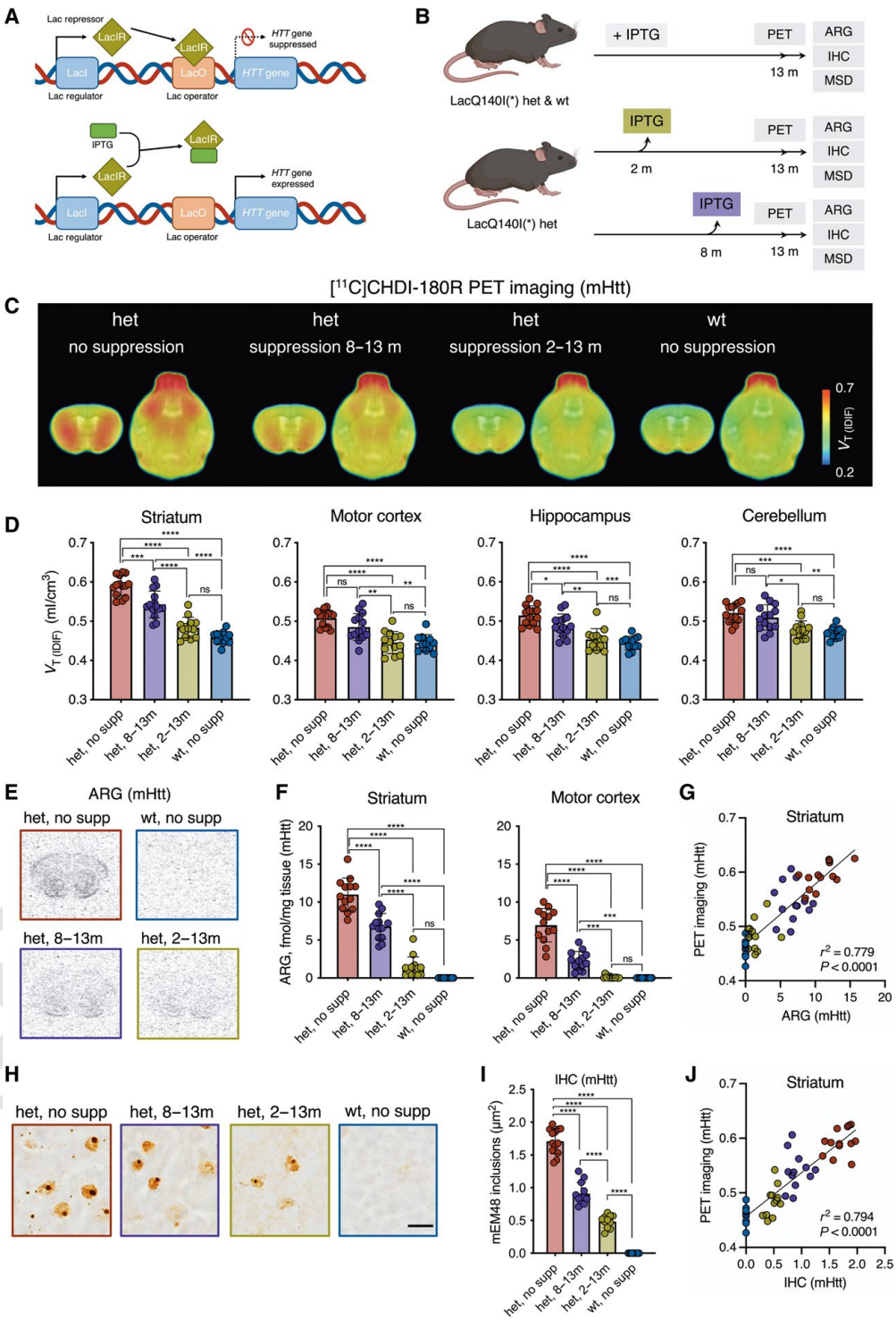

Fig. 5. Modulation of [^{11}C]CHDI-180R binding by broadly distributed mHTT lowering in LacQ140^{I}(*) het mice. (**A**) Schematic overview of the LacQ140^{I}(*) allele. The transcriptional repressor, LacIR, binds to the Lac operator, LacO, precluding expression of the Q140 allele (top). Administration of isopropyl-β-D-thiogalactopyranoside (IPTG) allosterically inhibits LacIR, allowing transcription of the Q140 allele. (**B**) Timeline overview and endpoints in LacQ140^{I}(*) wt and het mice. (**C**) Mean [^{11}C]CHDI-180R $V_{T\ (IDIF)}$ parametric images of LacQ140^{I}(*) wt and het mice at 13 months of age. PET images are coregistered to the MRI template for anatomical reference. Coronal and axial planes are shown. (**D**) Regional [^{11}C]CHDI-180R $V_{T\ (IDIF)}$ quantification in LacQ140^{I}(*) wt and het at 13 months (het no supp, $n = 14$; het 8–13m, $n = 14$; het 2–13m, $n = 13$; wt no supp, $n = 11$) of age. One-way ANOVA with Tukey's multiple comparison test. (**E** and **H**) Representative autoradiograms showing total binding of [^{3}H]CHDI-00485180 (mHTT inclusions) (E) and immunostaining as demonstrated by mEM48 (H) in LacQ140^{I}(*) wt and het mice. Scale bar, 10 μm. (**F** and **I**) Specific binding of [^{3}H]CHDI-00485180 (F) and quantification of inclusions for mEM48 (I) in LacQ140^{I}(*) wt and het mice at 13 months of age (het no supp, $n = 13$; het 8–13m, $n = 13$; het 2–13m, $n = 13$; wt no supp, $n = 12$). One-way ANOVA with Tukey's multiple comparison test. (**G**) Correlation between striatal mHTT binding measured with microPET and ARG in LacQ140^{I}(*) wt and het mice at 13 months of age. Two-tailed Pearson correlation analysis; $R^2 = 0.779$; $P < 0.0001$. (**J**) Correlation between striatal mHTT binding measured with microPET and immunostaining in LacQ140^{I}(*) wt and het mice at 13 months of age. Two-tailed Pearson correlation analysis; $R^2 = 0.794$; $P < 0.0001$. Data are shown as means ± SD; all points shown; $^{*}P < 0.05$, $^{**}P < 0.01$, $^{***}P < 0.001$, and $^{****}P < 0.0001$.

because we measured an average of 38% AAV-ZFP–transduced cells along the rostro-caudal axis, after AAV ZFP and ΔDBD-ZFP injections (fig. S10). We analyzed several brains to confirm the extent of ZFP distribution and its impact on mHTT aggregate number and intensity using mEM48 IHC. In the early treatment paradigm, the striatal region expressing the AAV ZFP treatment did not display any mHTT nuclear inclusions at 10 months of age (8 months of treatment) unlike the ZFP nontransduced region or contralateral ΔDBD-ZFP–injected hemisphere (fig. S11, A and B). In contrast, in the late treatment paradigm, smaller and fewer intranuclear mHTT inclusions are present after the AAV ZFP treatment than in the ZFP nontransduced area or the contralateral ΔDBD-ZFP–injected hemisphere (fig. S11, C and D). There was no evidence of microglial or astrocytic reactivity in the striatum of injected animals, as judged by Iba1 and GFAP (glial fibrillary acidic protein) reactivity (fig. S12), recapitulating what we reported in Zeitler *et al.* (*12*).

Collectively, these observations suggest that we achieve a 40% mHTT reduction in the early intervention paradigm and that this value is determined by the extent of neuronal transduction and viral distribution in the mouse striatum (38%). This value is in concordance

with the 38.9% signal decrease, measured in vivo using PET, with [^{11}C]CHDI-180R. In contrast, in the late intervention paradigm, and consistent with residual preexisting aggregate pathology that remains after AAV-ZFP administration after disease onset, we only achieved a 23.6% therapeutic effect as measured in vivo with [^{11}C]CHDI-180R at 10 months of age.

[^{11}C]CHDI-180R PET imaging detects widespread suppression of mHTT in the regulatable mHTT KI LacQ140^{I}(*) mouse model

Current clinical HTT-lowering directed therapeutic strategies are seeking to explore what degree of HTT reduction may produce clinical benefit in cortical and striatal regions, with several clinical programs targeting a 50% reduction (*5*, *6*, *11*, *38*, *39*). Therefore, we wanted to detect CNS-wide changes in mHTT within the range being pursued clinically, using a newly characterized KI LacQ140^{I}(*) mouse model, which allows for m*Htt* lowering in a regulatable fashion to about 40 to 50% throughout the body in a Q140 KI context (*40*). Because of the presence of the LacO repressor binding sites, the exposure to IPTG (isopropyl-β-D-thiogalactopyranoside) enables (derepresses) the expression of mHTT. Upon withdrawal of IPTG, mHTT expression is suppressed throughout the organism (Fig. 5 and fig. S9, G to I). The extent of mHTT aggregated species, as judged by MSD assays with MW8-4C9 (fig. S9H), depends on the timing of mHTT mRNA suppression.

We used this model to lower m*Htt* systemically at 2 or 8 months of age, before and after mHTT inclusion formation and disease onset, and compared them to control mice or LacQ140^{I}(*) mice with m*Htt* expressed throughout its life, at 13 months of age (Fig. 5, A and B, and table S7). [^{11}C]CHDI-180R $V_{T\,(IDIF)}$ values were reduced consistently with suppression duration in all brain regions examined after IPTG withdrawal before (2 to 13 months) and after (8 to 13 months) mHTT inclusion formation (Fig. 5, C and D). The estimated mHTT suppression effect was calculated according to Eq. 2 (see Materials and Methods) as the difference between het mice subjected to m*Htt* lowering (either as of 2 or 8 months) and het mice without m*Htt* suppression. This difference was normalized to the total genotypic difference, estimated as the delta between het, no suppression (total signal) and wt, no suppression mice (nondisplaceable signal). We estimated a global 80 to 95% or 20 to 35% mHTT aggregate lowering after IPTG withdrawal at 2 or 8 months (treatment effect striatum: $F_{3,48} = 62.30$, $P < 0.0001$). The apparent disconnect between the 40 and 50% m*Htt* lowering in this model and the 80 to 95% mHTT lowering measured with [^{11}C]CHDI-180R in the early intervention study suggests that a modulation of 40 to 50% of m*Htt* expression before aggregate formation might be sufficient to largely avoid or delay the generation of [^{11}C]CHDI-180R–binding species.

Consistently, autoradiographic [^{3}H]CHDI-180 binding was significantly reduced (striatum, $F_{3,47} = 133.80$, $P < 0.0001$; Fig. 5, E and F), demonstrating agreement with [^{11}C]CHDI-180R PET ($R^2 = 0.779$, $P < 0.0001$; Fig. 5G). The extent of mHTT lowering was supported by mEM48 immunostaining ($F_{3,46} = 360.80$, $P < 0.0001$; Fig. 5, H and I), in line with the [^{11}C]CHDI-180R binding ($R^2 = 0.794$, $P < 0.0001$; Fig. 5J), as well as MSD measurements of HTT using cerebellar extracts obtained from the same animals ($P < 0.05$ to $P < 0.0001$; fig. S9, G to I).

DISCUSSION

Several therapeutic studies targeting HTT expression are being evaluated or planned in clinical studies (*5*, *6*, *11*, *38*, *39*). Given the different therapeutic modalities leading to distinct restricted distribution patterns, an understanding of the regional effects of HTT lowering agents is fundamental for interpreting, and improving upon, clinical trial results. It is in this context that we set out to develop a strategy to identify and characterize potential indicators that can help guide the clinical development of HTT lowering agents. Here, we extend our prior characterization of CHDI-180R and demonstrate the time- and region-dependent appearance of mHTT pathology in the HD mouse models R6/2, HdhQ80, and zQ175DN. The ligand is suitable to detect genotype- and region-specific differences in mHTT pathology throughout the brain, allowing for its deployment in therapeutic studies with manageable sample size and a longitudinal manner. We were able to ascertain different regional pathology within the striatum, particularly in HdhQ80 mice, which appears to proceed from a ventral to dorsal trajectory, an observation reminiscent of human pathology that proceeds caudal-to-rostral and dorsal-to-ventral (*2*, *3*).

We applied [^{11}C]CHDI-180R in two interventional paradigms when mHTT is lowered in a restricted manner in the striatum of mice, or more broadly throughout the mouse brain, within the range of mHTT suppression expected in clinical studies (~50%). The extent of lowering detected by [^{11}C]CHDI-180R correlates well with the extent of mHTT suppression as measured by quantitative assays for soluble and aggregated forms of mHTT. These studies show that [^{11}C]CHDI-180R could potentially be used irrespective of the regional distribution of the therapeutic agents or the extent of lowering. Furthermore, we verified the extent of lowering by ARG, showing excellent concordance with PET imaging. In the context of the ZFP repressor, the decrease in the signal obtained with [^{11}C]CHDI-180R appears rapid (1 month after administration of AAV-ZFP) and is sustained during the duration of the studies (up to 8 months). When administered early, before the appearance of pathology, AAV-ZFP prevents mHTT inclusion and extranuclear aggregation, and the decrease of the signal detected by [^{11}C]CHDI-180R might be explained by the extent of agent distribution and neuronal transduction (in our case, about 40% of the striatum).

A number of considerations and limitations should be highlighted to appropriately interpret the findings. First, we do not yet have a full understanding of the various species of mHTT that constitute the binding site(s) for CHDI-180. Nonetheless, based on previous in vitro studies (*8*, *9*), we know that this ligand can bind oligomerized mHTT and some forms of fibrillar mHTT but not to monomeric soluble HTT. Besides our poor understanding of the precise states of mHTT to which CHDI-180 binds to, adequate information on the dynamics between the soluble and aggregated pools of mHTT is similarly lacking. We expect that the availability of this PET tracer in parallel to biofluid readouts for HTT, like mass spectrometry and quantitative MSD/single-molecule counting, may facilitate a better understanding of how these different pools of mHTT are handled in brain cells, and how the extent of mHTT lowering may shift the dynamics of such cellular processes. Second, mHTT concentration has been measured clinically using a 2B7/MW1 immunoassay (*5*); therefore, comparing the extent of lowering of soluble amount of mHTT using 2B7/MW1 in CSF to the spinal mHTT as well as the extent of parenchymal changes observed with [^{11}C]CHDI-180R would be desirable. However, method development for mouse CSF mHTT detection remains difficult and samples were not collected in this work. However, a disconnect between the extent of lowering of mHTT in CSF as compared to caudate/putamen suppression concentration after AAV5–AMT-130 administration was recently shown in an mHTT

transgenic minipig model (*7*). Third, mHTT accumulates in all brain structures; thus, measurement of input function for [^{11}C]CHDI-180R quantification is necessary. Because arterial blood sampling in mice represents a very challenging and end-of-life procedure, we exploited the use of a cardiac IDIF for noninvasive quantification (*24*, *25*). Although this approach might be sensitive to over- or underestimation of the blood activity (*41*), it is suitable to perform reliable comparative studies as shown in previous work (*42*–*44*) as well as indicated by the measurement stability in same animals over time and confirmed across different studies. This limitation will not apply to larger animal models and humans, where arterial blood sampling is feasible. Fourth, PET imaging of mHTT density was measured with V_T, which comprises both specific and nondisplaceable binding, whereas PDE10a, D_1R, and $D_{2/3}$R could be quantified with BP_{ND}, a direct measure of target density, given the presence of a reference region (*26*). Therefore, any change measured in V_T is intrinsically smaller than with BP_{ND}, an important aspect to consider for adequate comparison across markers. Overall, given the long half-life of mHTT protein and the impact that preexisting aggregate pathology can have in establishing an adequate experimental design, future studies will be needed to obtain a detailed understanding of the effects of different therapeutic agents targeting mHTT DNA or RNA on both soluble and aggregated amounts in terms of type, timing, and magnitude of responsiveness during the disease course.

We investigated potential striatal markers that can serve as markers of functional SPN restoration. Several PET ligands, previously shown to track disease progression in HD individuals, have been shown to track progression in models of HD (*33*–*35*, *43*, *45*). We show that the response to mHTT lowering in SPNs is fast and durable, and that these effects can be observed even in the context of established disease and aging, at least in the zQ175DN model. During the early intervention paradigm, all striatal markers responded within a month of therapy, suggesting an improvement of cellular alterations in indirect-pathway SPNs (expressing both PDE10 and D_2R) and direct-pathway neurons (expressing PDE10 and D_1R). When AAV-ZFP is administered after disease onset, the response is more muted, but present for all tracers, particularly as judged by ARG, which has a higher signal-to-background ratio than microPET. PDE10a and D_1R expression appears more responsive to mHTT lowering than does $D_{2/3}$R, arguing that direct-pathway neurons (affected later in the disease) might be more amenable to functional restoration.

The strong correlation seen in intra-animal comparisons between [^{11}C]CHDI-180R and PDE10a binding across our cohorts strongly supports the concept that PDE10a imaging may be a sensitive translational marker of early therapeutic benefit, whether from mHTT lowering or any other intervention that restores striatal projection function. As this marker is one of the earliest markers altered in premanifest individuals, including those far from disease onset (*15*–*17*), PDE10a imaging can be used to track functional responses to HTT lowering in prodromal clinical studies.

In summary, we demonstrated the development of a small-molecule PET ligand with high affinity and selectivity for mHTT to monitor noninvasively mHTT pathology in the living brain and track region- and time-dependent suppression of mHTT amount in response to therapeutic intervention. We also showed that therapeutic agents, such as AAV-ZFP, can be functionally restorative and their effects can be measured by the preservation of striatal imaging markers. The ability to measure time- and region-specific effects of agents that suppress HTT expression will be extremely informative to understand the pharmacodynamic effects and clinical impact of experimental gene therapy and small-molecule agents being evaluated in clinical trials.

MATERIALS AND METHODS

Study design

The objective of this study was to investigate the utility of the high affinity and selectivity for mHTT PET ligand [^{11}C]CHDI-180R to detect mHTT aggregation in affected brain cells and its application as indicator of pharmacological activity of agents that target HTT expression in the living brain. We first performed ARG and IHC analysis on brain samples from postmortem human tissue as well as zQ175DN, HdhQ80, and R6/2 HD models and age-matched wt mice to explore signal concentration and pattern. Next, we carried out a longitudinal study to characterize [^{11}C]CHDI-180R PET imaging to enable noninvasive monitoring of mHTT pathology in the brain and spinal cord of untreated wt and het zQ175DN mice. This work was used to quantify [^{11}C]CHDI-180R binding at different disease stages and perform power analysis for adequate sample sizes in therapeutic interventions lowering mHTT concentration. With the aim of determining whether [^{11}C]CHDI-180R could track region- and time-dependent suppression of mHTT in response to therapeutic interventions targeting mHTT expression, we performed longitudinal studies in zQ175DN mice with a ZFP-based therapeutic intervention as well as in the regulatable LacQ140^{I}(*) mouse model. The sample size was calculated for all in vivo cross-sectional and longitudinal studies to provide 80% statistical power with a type 1 error rate of 0.05 in detecting changes of PET imaging readouts. No prior power analysis was performed for in vitro studies, but sample size resulted to be adequate for the aim of the analyses. Investigators performing the longitudinal therapeutic studies were blinded to treatment condition until completion of studies. Randomization was applied to each experiment. No samples correctly acquired were excluded from the study.

PET imaging

Image acquisition

Dynamic microPET/computed tomography (CT) images were acquired using two virtually identical Siemens Inveon PET/CT scanners (Siemens Preclinical Solution) as previously described (*25*, *35*, *44*). Animals were anesthetized using isoflurane in medical oxygen (induction 5%, maintenance 1.5%) and catheterized in the tail vein for intravenous bolus injection of the tracer. Animals were placed on the scanner bed with the full body in the PET scanner's field of view to allow the extraction of the IDIF from the left ventricle as previously described (*24*, *25*). Bolus injection of radiotracer occurred over a 12-s interval (1 ml/min) using an automated pump (Pump 11 Elite, Harvard Apparatus) at the onset of the dynamic microPET scan. Information regarding molar activity injected radioactivity, injected mass, body weight, and age on scan day for each radioligand at different time points and studies are reported in tables S1, S4, and S5 to S7. Radioligands were injected with activity as high as possible to obtain good image quality and keeping the cold mass as low as possible in order not to violate tracer conditions. We experimentally measured and characterized the mass-dose effect for the various tracers. In all experimental paradigms, we stayed well below the critical limit and set our target at 1.25 μg/kg for [^{11}C]CHDI-180R, 1 μg/kg for [^{18}F]MNI-659, 2 μg/kg for [^{11}C]SCH23390, and 1.5 μg/kg for [^{11}C]Raclopride. PET data were acquired in list mode format. Dynamic scans lasted 60 min for [^{11}C]CHDI-180R and [^{11}C]Raclopride,

whereas a 90-min acquisition was performed for [^{18}F]MNI-659 and [^{11}C]SCH23390. PET scans were followed by a 10-min 80-kV/500-μA CT scan on the same gantry for attenuation correction and coregistration purposes. Acquired PET data were reconstructed into 33 or 39 (for 60- or 90-min acquisition, respectively) frames of increasing length (12 × 10s, 3 × 20s, 3 × 30s, 3 × 60s, 3 × 150s, and 9 or 15 × 300s) using a list-mode iterative reconstruction with proprietary spatially variant resolution modeling in 8 iterations and 16 subsets of the three-dimensional (3D) ordered subset expectation maximization (OSEM 3D) algorithm (*46*). Normalization, dead time, and CT-based attenuation corrections were applied. PET image frames were reconstructed on a 128 × 128 × 159 grid with 0.776 × 0.776 × 0.796 mm^3 voxels.

Image processing

Image analysis was performed with PMOD 3.6 software (PMOD Technologies) applying a CT-based pipeline for the longitudinal natural history study and a magnetic resonance (MR)–based pipeline for the therapeutic and LacQ140^{I}(*) studies. When we applied the CT-based pipeline, spatial normalization of the PET/CT images was done through brain normalization of the CT image to the CT/MR imaging (MRI) template with predefined volumes of interest (VOIs) adapting the previously described procedure (*34*). The spatial transformations were applied to the dynamic PET images and assessed for accuracy after spatial transformation. Using the VOI template adapted from the Waxholm atlas (*47*) (as shown in fig. S3), time-activity curves (TACs) for the striatum, motor cortex, hippocampus, thalamus, and cerebellum were extracted from the dynamic PET images to perform kinetic modeling.

Because we previously observed that the use of MRI templates for spatial normalization and VOI definition improves the accuracy of the regional quantification of PET data with focal uptake, the therapeutic and LacQ140^{I}(*) studies were processed using an MR-based pipeline (*34*). VOIs were manually adapted from the Waxholm atlas (*47*) to match each genotype- and age-specific MR template. TACs for the striatum, motor cortex, hippocampus, thalamus, and cerebellum were extracted from the dynamic PET images to perform kinetic modeling. For analysis of spinal cord, VOIs were manually drawn on the individual CT images, and TACs were extracted from the dynamic scans for regional quantification.

Kinetic modeling

In zQ175DN and Q140 mouse models, mHTT accumulates in all brain structures (*8*, *14*, *20*, *40*) and no suitable reference region for relative quantification could be identified. Hence, absolute quantification for [^{11}C]CHDI-180R was performed to calculate the total volume of distribution based on IDIF [$V_{T\,(IDIF)}$] as a noninvasive surrogate of V_T. Kinetic modeling fitted regional TACs using the Logan model (*27*) and the IDIF with the start of the linear regression (t^*) calculated according to the maximum error criterion of 10%. The IDIF was obtained from the whole-blood activity derived from the PET images by generating a region of interest (threshold-based 50% of max) in the lumen of the left ventricle as previously described (*24*, *25*). Because only negligible metabolism of [^{11}C]CHDI-180R was observed in different genotypes and ages (parent compound >95%), no correction for radiometabolites was applied.

Parametric $V_{T\,(IDIF)}$ maps were generated through voxel-based graphical analysis (Logan) (*27*) using the IDIF as input function and were then cropped using the brain mask of the MRI template, represented as group averages, and overlaid onto a 3D mouse brain template for anatomical reference. Individual images were smoothed with an isotropic Gaussian filter (0.5 mm in full width at half maximum).

For the longitudinal natural history study, voxel-based analysis with Statistical Parametric Mapping (SPM) using SPM12 (Wellcome Centre for Human Neuroimaging) was performed on het zQ175DN mice to evaluate the voxel-based changes with disease progression. Data from zQ175DN het mice were compared between time points to determine longitudinal changes in [^{11}C]CHDI-180R $V_{T\,(IDIF)}$. Statistical t maps were generated for a peak voxel threshold of $P = 0.01$ (uncorrected) and a cluster threshold of 10 voxels (0.8 mm^3). Only significant clusters with $P < 0.01$ were considered.

For the quantification of [^{18}F]MNI-659, [^{11}C]SCH23390, and [^{11}C]Raclopride, the binding potential (BP_{ND}) was determined by fitting the regional TACs using the simplified reference tissue modeling (SRTM) (*48*). The striatum was selected as the receptor-rich region, and the cerebellum was selected as the receptor-free region (reference region) (*34*, *35*). Parametric BP_{ND} maps were generated using SRTM2 (*49*) with k_2' as calculated with SRTM (*48*). The individual images were smoothed with an isotropic Gaussian filter (0.5 mm in full width at half maximum), cropped using the brain mask of the MRI template, represented as group averages, and overlaid onto each condition- and age-specific 3D brain template for anatomical reference.

Because ZFP delivery was restricted to the ipsilateral striatum, the therapeutic response of each molecular target in the early and late ZFP intervention studies was estimated as follows according to Figs. 3B and 4B

$$\text{Therapeutic response}\,(\%) = \frac{\text{ZFP}_{(\text{LSTR treated het})} - \Delta\text{DBD}_{(\text{RSTR treated het})}}{\Delta\text{DBD}_{(\text{wt})} - \Delta\,\text{DBD}_{(\text{RSTR treated\&control het})}} * 100 \quad (1)$$

where LSTR and RSTR represent the left and right striatum, respectively.

In the LacQ140^{I}(*) studies, the mHTT lowering response of [^{11}C]CHDI-180R was estimated as follows

$$\text{mHTT lowering response}\,(\%) = \frac{\text{HET}_{(2\text{–or }8\text{–}13\text{m supp})} - \text{HET}_{(\text{no supp})}}{\text{HET}_{(\text{no supp})} - \text{WT}_{(\text{no supp})}} * 100 \quad (2)$$

Statistical analysis

Statistical analysis was performed in GraphPad Prism v9.1 (GraphPad Software) and JMP Pro 14 (SAS Institute Inc.). Data are expressed as means ± SD unless otherwise indicated in the figure legends. To choose the appropriate statistical test, data were checked for normality using the Shapiro-Wilk test. If the normality test was not passed, nonparametric statistical tests were used. Longitudinal analysis of each PET readout was performed using linear mixed-effects models, with each radioligand quantification as the primary endpoint. Genotype, cohort, time point, region, and treatment (when applicable) were considered as fixed factors, with subjects as a random effect. Interaction effects (genotype*time, cohort*time, treatment*time, and treatment*region) were evaluated as well. Comparisons were performed to evaluate regional temporal and genotypic differences as well as treatment effects. Correlation coefficients were calculated with Pearson's correlation analysis. Sample size calculations at desired therapeutic effects were performed in G*Power software (www.gpower.hhu.de/). Statistical significance was set at $P < 0.05$, with the following standard abbreviations used to reference P values: ns, not significant; *$P < 0.05$; **$P < 0.01$; ***$P < 0.001$; ****$P < 0.0001$. Detailed statistical information for each experiment is provided in the corresponding figure legends.

AQ6

SUPPLEMENTARY MATERIALS

www.science.org/doi/10.1126/scitranslmed.abm3682
Materials and Methods
Figs. S1 to S12
Tables S1 to S11
Data file S1
References (*50*–*54*)

View/request a protocol for this paper from *Bio-protocol*.

REFERENCES AND NOTES

1. The Huntington's Disease Collaborative Research Group, A novel gene containing a trinucleotide repeat that is expanded and unstable on Huntington's disease chromosomes. *Cell* **72**, 971–983 (1993).
2. H. J. Waldvogel, E. H. Kim, L. J. Tippett, J. P. Vonsattel, R. L. Faull, The neuropathology of Huntington's disease. *Curr. Top. Behav. Neurosci.* **22**, 33–80 (2015).
3. U. Rub, J. P. Vonsattel, H. Heinsen, H. W. Korf, The neuropathology of Huntington's disease: Classical findings, recent developments and correlation to functional neuroanatomy. *Adv. Anat. Embryol. Cell Biol.* **217**, 1–146 (2015).
4. H. B. Kordasiewicz, L. M. Stanek, E. V. Wancewicz, C. Mazur, M. M. McAlonis, K. A. Pytel, J. W. Artates, A. Weiss, S. H. Cheng, L. S. Shihabuddin, G. Hung, C. F. Bennett, D. W. Cleveland, Sustained therapeutic reversal of Huntington's disease by transient repression of huntingtin synthesis. *Neuron* **74**, 1031–1044 (2012).
5. S. J. Tabrizi, B. R. Leavitt, G. B. Landwehrmeyer, E. J. Wild, C. Saft, R. A. Barker, N. F. Blair, D. Craufurd, J. Priller, H. Rickards, A. Rosser, H. B. Kordasiewicz, C. Czech, E. E. Swayze, D. A. Norris, T. Baumann, I. Gerlach, S. A. Schobel, E. Paz, A. V. Smith, C. F. Bennett, R. M. Lane; Phase 1–2a IONIS-HTTRx Study Site Teams, Targeting huntingtin expression in patients with Huntington's disease. *N. Engl. J. Med.* **380**, 2307–2316 (2019).
6. E. A. Spronck, A. Valles, M. H. Lampen, P. S. Montenegro-Miranda, S. Keskin, L. Heijink, M. M. Evers, H. Petry, S. J. van Deventer, P. Konstantinova, M. Haan, Intrastriatal administration of AAV5-miHTT in non-human primates and rats is well tolerated and results in miHTT transgene expression in key areas of Huntington disease pathology. *Brain Sci.* **11**, 129 (2021).
7. A. Valles, M. M. Evers, A. Stam, M. Sogorb-Gonzalez, C. Brouwers, C. Vendrell-Tornero, S. Acar-Broekmans, L. Paerels, J. Klima, B. Bohuslavova, R. Pintauro, V. Fodale, A. Bresciani, R. Liscak, D. Urgosik, Z. Starek, M. Crha, B. Blits, H. Petry, Z. Ellederova, J. Motlik, S. van Deventer, P. Konstantinova, Widespread and sustained target engagement in Huntington's disease minipigs upon intrastriatal microRNA-based gene therapy. *Sci. Transl. Med.* **13**, (2021).
8. L. Liu, M. E. Prime, M. R. Lee, V. Khetarpal, C. J. Brown, P. D. Johnson, P. Miranda-Azpiazu, X. Chen, D. Clark-Frew, S. Coe, R. Davis, A. Dickie, A. Ebneth, S. Esposito, E. Gadouleau, X. Gai, S. Galan, S. Green, C. Greenaway, P. Giles, C. Halldin, S. Hayes, T. Herbst, F. Herrmann, M. Hessmann, Z. Jia, A. Kiselyov, A. Kotey, T. Krulle, J. E. Mangette, R. W. Marston, S. Menta, M. R. Mills, E. Monteagudo, S. Nag, M. Nibbio, L. Orsatti, S. Schaertl, C. Scheich, J. Sproston, V. Stepanov, M. Svedberg, A. Takano, M. Taylor, W. Thomas, M. Toth, D. Vaidya, K. Vanras, D. Weddell, I. Wigginton, J. Wityak, L. Mrzljak, I. Munoz-Sanjuan, J. A. Bard, C. Dominguez, Imaging mutant Huntingtin aggregates: Development of a potential PET ligand. *J. Med. Chem.* **63**, 8608–8633 (2020).
9. F. Herrmann, M. Hessmann, S. Schaertl, K. Berg-Rosseburg, C. J. Brown, G. Bursow, A. Chiki, A. Ebneth, M. Gehrmann, N. Hoeschen, M. Hotze, S. Jahn, P. D. Johnson, V. Khetarpal, A. Kiselyov, K. Kottig, S. Ladewig, H. Lashuel, S. Letschert, M. R. Mills, K. Petersen, M. E. Prime, C. Scheich, G. Schmiedel, J. Wityak, L. Liu, C. Dominguez, I. Munoz-Sanjuan, J. A. Bard, Pharmacological characterization of mutant huntingtin aggregate-directed PET imaging tracer candidates. *Sci. Rep.* **11**, 17977 (2021).
10. D. Bertoglio, J. Verhaeghe, A. Miranda, L. Wyffels, S. Stroobants, L. Mrzljak, V. Khetarpal, M. Skinbjerg, L. Liu, C. Dominguez, I. Munoz-Sanjuan, J. Bard, S. Staelens, Longitudinal preclinical evaluation of the novel radioligand [^{11}C]CHDI-626 for PET imaging of mutant huntingtin aggregates in Huntington's disease. *Eur. J. Nucl. Med. Mol. Imaging*, (2021).
11. S. J. Tabrizi, M. D. Flower, C. A. Ross, E. J. Wild, Huntington disease: New insights into molecular pathogenesis and therapeutic opportunities. *Nat. Rev. Neurol.* **16**, 529–546 (2020).
12. B. Zeitler, S. Froelich, K. Marlen, D. A. Shivak, Q. Yu, D. Li, J. R. Pearl, J. C. Miller, L. Zhang, D. E. Paschon, S. J. Hinkley, I. Ankoudinova, S. Lam, D. Guschin, L. Kopan, J. M. Cherone, H. B. Nguyen, G. Qiao, Y. Ataei, M. C. Mendel, R. Amora, R. Surosky, J. Laganiere, B. J. Vu, A. Narayanan, Y. Sedaghat, K. Tillack, C. Thiede, A. Gartner, S. Kwak, J. Bard, L. Mrzljak, L. Park, T. Heikkinen, K. K. Lehtimaki, M. M. Svedberg, J. Haggkvist, L. Tari, M. Toth, A. Varrone, C. Halldin, A. E. Kudwa, S. Ramboz, M. Day, J. Kondapalli, D. J. Surmeier, F. D. Urnov, P. D. Gregory, E. J. Rebar, I. Munoz-Sanjuan, H. S. Zhang, Allele-selective transcriptional repression of mutant *HTT* for the treatment of Huntington's disease. *Nat. Med.* **25**, 1131–1142 (2019).
13. T. Heikkinen, K. Lehtimaki, N. Vartiainen, J. Puolivali, S. J. Hendricks, J. R. Glaser, A. Bradaia, K. Wadel, C. Touller, O. Kontkanen, J. M. Yrjanheikki, B. Buisson, D. Howland, V. Beaumont, I. Munoz-Sanjuan, L. C. Park, Characterization of neurophysiological and behavioral changes, MRI brain volumetry and 1H MRS in zQ175 knock-in mouse model of Huntington's disease. *PLOS ONE* **7**, e50717 (2012).
14. L. B. Menalled, A. E. Kudwa, S. Miller, J. Fitzpatrick, J. Watson-Johnson, N. Keating, M. Ruiz, R. Mushlin, W. Alosio, K. McConnell, D. Connor, C. Murphy, S. Oakeshott, M. Kwan, J. Beltran, A. Ghavami, D. Brunner, L. C. Park, S. Ramboz, D. Howland, Comprehensive behavioral and molecular characterization of a new knock-in mouse model of Huntington's disease: zQ175. *PLOS One* **7**, e49838 (2012).
15. D. S. Russell, D. L. Jennings, O. Barret, G. D. Tamagnan, V. M. Carroll, F. Caille, D. Alagille, T. J. Morley, C. Papin, J. P. Seibyl, K. L. Marek, Change in PDE10 across early Huntington disease assessed by [18F]MNI-659 and PET imaging. *Neurology* **86**, 748–754 (2016).
16. V. Beaumont, S. Zhong, H. Lin, W. Xu, A. Bradaia, E. Steidl, M. Gleyzes, K. Wadel, B. Buisson, F. E. Padovan-Neto, S. Chakroborty, K. M. Ward, J. F. Harms, J. Beltran, M. Kwan, A. Ghavami, J. Haggkvist, M. Toth, C. Halldin, A. Varrone, C. Schaab, J. N. Dybowski, S. Elschenbroich, K. Lehtimaki, T. Heikkinen, L. Park, J. Rosinski, L. Mrzljak, D. Lavery, A. R. West, C. J. Schmidt, M. M. Zaleska, I. Munoz-Sanjuan, Phosphodiesterase 10A inhibition improves cortico-basal ganglia function in Huntington's disease models. *Neuron* **92**, 1220–1237 (2016).
17. P. Fazio, C. J. Fitzer-Attas, L. Mrzljak, J. Bronzova, S. Nag, J. H. Warner, B. Landwehrmeyer, N. Al-Tawil, C. Halldin, A. Forsberg, J. Ware, V. Dilda, A. Wood, C. Sampaio, A. Varrone; PEARL-HD and LONGPDE10 study collaborators, PET molecular imaging of phosphodiesterase 10A: An early biomarker of Huntington's disease progression. *Mov. Disord.* **35**, 606–615 (2020).
18. R. A. Weeks, P. Piccini, A. E. Harding, D. J. Brooks, Striatal D1 and D2 dopamine receptor loss in asymptomatic mutation carriers of Huntington's disease. *Ann. Neurol.* **40**, 49–54 (1996).
19. A. Antonini, K. L. Leenders, D. Eidelberg, [^{11}C]raclopride-PET studies of the Huntington's disease rate of progression: Relevance of the trinucleotide repeat length. *Ann. Neurol.* **43**, 253–255 (1998).
20. N. Carty, N. Berson, K. Tillack, C. Thiede, D. Scholz, K. Kottig, Y. Sedaghat, C. Gabrysiak, G. Yohrling, H. von der Kammer, A. Ebneth, V. Mack, I. Munoz-Sanjuan, S. Kwak, Characterization of HTT inclusion size, location, and timing in the zQ175 mouse model of Huntington's disease: An in vivo high-content imaging study. *PLOS ONE* **10**, e0123527 (2015).
21. P. Langfelder, J. P. Cantle, D. Chatzopoulou, N. Wang, F. Gao, I. Al-Ramahi, X. H. Lu, E. M. Ramos, K. El-Zein, Y. Zhao, S. Deverasetty, A. Tebbe, C. Schaab, D. J. Lavery, D. Howland, S. Kwak, J. Botas, J. S. Aaronson, J. Rosinski, G. Coppola, S. Horvath, X. W. Yang, Integrated genomics and proteomics define huntingtin CAG length-dependent networks in mice. *Nat. Neurosci.* **19**, 623–633 (2016).
22. C. A. Gutekunst, S. H. Li, H. Yi, J. S. Mulroy, S. Kuemmerle, R. Jones, D. Rye, R. J. Ferrante, S. M. Hersch, X. J. Li, Nuclear and neuropil aggregates in Huntington's disease: Relationship to neuropathology. *J. Neurosci.* **19**, 2522–2534 (1999).
23. J. Ko, J. M. Isas, A. Sabbaugh, J. H. Yoo, N. K. Pandey, A. Chongtham, M. Ladinsky, W. L. Wu, H. Rohweder, A. Weiss, D. Macdonald, I. Munoz-Sanjuan, R. Langen, P. H. Patterson, A. Khoshnan, Identification of distinct conformations associated with monomers and fibril assemblies of mutant huntingtin. *Hum. Mol. Genet.* **27**, 2330–2343 (2018).
24. J. Verhaeghe, D. Bertoglio, L. Kosten, D. Thomae, M. Verhoye, A. Van Der Linden, L. Wyffels, S. Stroobants, J. Wityak, C. Dominguez, L. Mrzljak, S. Staelens, Noninvasive relative quantification of [^{11}C]ABP688 PET imaging in mice versus an input function measured over an arteriovenous shunt. *Front. Neurol.* **9**, 516 (2018).
25. D. Bertoglio, J. Verhaeghe, S. Korat, A. Miranda, L. Wyffels, S. Stroobants, L. Mrzljak, C. Dominguez, L. Liu, M. Skinbjerg, I. Munoz-Sanjuan, S. Staelens, In vitro and in vivo assessment of suitable reference region and kinetic modelling for the mGluR1 radioligand [^{11}C]ITDM in mice. *Mol. Imaging Biol.* **22**, 854–863 (2020).
26. R. B. Innis, V. J. Cunningham, J. Delforge, M. Fujita, A. Gjedde, R. N. Gunn, J. Holden, S. Houle, S. C. Huang, M. Ichise, H. Iida, H. Ito, Y. Kimura, R. A. Koeppe, G. M. Knudsen, J. Knuuti, A. A. Lammertsma, M. Laruelle, J. Logan, R. P. Maguire, M. A. Mintun, E. D. Morris, R. Parsey, J. C. Price, M. Slifstein, V. Sossi, T. Suhara, J. R. Votaw, D. F. Wong, R. E. Carson, Consensus nomenclature for in vivo imaging of reversibly binding radioligands. *J. Cereb. Blood Flow Metab.* **27**, 1533–1539 (2007).
27. J. Logan, J. S. Fowler, N. D. Volkow, A. P. Wolf, S. L. Dewey, D. J. Schlyer, R. R. MacGregor, R. Hitzemann, B. Bendriem, S. J. Gatley, D. R. Christman, Graphical analysis of reversible radioligand binding from time-activity measurements applied to [N-11C-methyl]-(–)-cocaine PET studies in human subjects. *J. Cereb. Blood Flow Metab.* **10**, 740–747 (1990).
28. B. Dehay, C. Weber, Y. Trottier, A. Bertolotti, Mapping of the epitope of monoclonal antibody 2B4 to the proline-rich region of human Huntingtin, a region critical for aggregation and toxicity. *Biotechnol. J.* **2**, 559–564 (2007).
29. G. Sciacca, F. Cicchetti, Mutant huntingtin protein expression and blood-spinal cord barrier dysfunction in huntington disease. *Ann. Neurol.* **82**, 981–994 (2017).
30. N. Pavese, M. Politis, Y. F. Tai, R. A. Barker, S. J. Tabrizi, S. L. Mason, D. J. Brooks, P. Piccini, Cortical dopamine dysfunction in symptomatic and premanifest Huntington's disease gene carriers. *Neurobiol. Dis.* **37**, 356–361 (2010).

31. T. C. Andrews, R. A. Weeks, N. Turjanski, R. N. Gunn, L. H. Watkins, B. Sahakian, J. R. Hodges, A. E. Rosser, N. W. Wood, D. J. Brooks, Huntington's disease progression. PET and clinical observations. *Brain* **122** (Pt. 12), 2353–2363 (1999).
32. C. C. Tang, A. Feigin, Y. Ma, C. Habeck, J. S. Paulsen, K. L. Leenders, L. K. Teune, J. C. van Oostrom, M. Guttman, V. Dhawan, D. Eidelberg, Metabolic network as a progression biomarker of premanifest Huntington's disease. *J. Clin. Invest.* **123**, 4076–4088 (2013).
33. J. Haggkvist, M. Toth, L. Tari, K. Varnas, M. Svedberg, A. Forsberg, S. Nag, C. Dominguez, I. Munoz-Sanjuan, J. Bard, J. Wityak, A. Varrone, C. Halldin, L. Mrzljak, Longitudinal small-animal PET imaging of the zQ175 mouse model of Huntington disease shows in vivo changes of molecular targets in the striatum and cerebral cortex. *J. Nucl. Med.* **58**, 617–622 (2017).
34. D. Bertoglio, J. Verhaeghe, L. Kosten, D. Thomae, A. Van der Linden, S. Stroobants, J. Wityak, C. Dominguez, L. Mrzljak, S. Staelens, MR-based spatial normalization improves [18F]MNI-659 PET regional quantification and detectability of disease effect in the Q175 mouse model of Huntington's disease. *PLOS ONE* **13**, e0206613 (2018).
35. D. Bertoglio, J. Verhaeghe, A. Miranda, L. Wyffels, S. Stroobants, C. Dominguez, I. Munoz-Sanjuan, M. Skinbjerg, L. Liu, S. Staelens, Kinetic modelling and test-retest reproducibility for the dopamine D_1R radioligand [^{11}C]SCH23390 in healthy and diseased mice. *Mol. Imaging Biol.* **23**, 208–219 (2021).
36. D. Macdonald, M. A. Tessari, I. Boogaard, M. Smith, K. Pulli, A. Szynol, F. Albertus, M. B. Lamers, S. Dijkstra, D. Kordt, W. Reindl, F. Herrmann, G. McAllister, D. F. Fischer, I. Munoz-Sanjuan, Quantification assays for total and polyglutamine-expanded huntingtin proteins. *PLOS ONE* **9**, e96854 (2014).
37. W. Reindl, B. Baldo, J. Schulz, I. Janack, I. Lindner, M. Kleinschmidt, Y. Sedaghat, C. Thiede, K. Tillack, C. Schmidt, I. Cardaun, T. Schwagarus, F. Herrmann, M. Hotze, G. F. Osborne, S. Herrmann, A. Weiss, C. Zerbinatti, G. P. Bates, J. Bard, I. Munoz-Sanjuan, D. Macdonald, Meso scale discovery-based assays for the detection of aggregated huntingtin. *PLOS ONE* **14**, e0213521 (2019).
38. E. A. Spronck, C. C. Brouwers, A. Valles, M. de Haan, H. Petry, S. J. van Deventer, P. Konstantinova, M. M. Evers, AAV5-miHTT gene therapy demonstrates sustained Huntingtin lowering and functional improvement in Huntington disease mouse models. *Mol. Ther. Methods Clin. Dev.* **13**, 334–343 (2019).
39. N. S. Caron, A. L. Southwell, C. C. Brouwers, L. D. Cengio, Y. Xie, H. F. Black, L. M. Anderson, S. Ko, X. Zhu, S. J. van Deventer, M. M. Evers, P. Konstantinova, M. R. Hayden, Potent and sustained huntingtin lowering via AAV5 encoding miRNA preserves striatal volume and cognitive function in a humanized mouse model of Huntington disease. *Nucleic Acids Res.* **48**, 36–54 (2020).
40. L. B. Menalled, J. D. Sison, I. Dragatsis, S. Zeitlin, M. F. Chesselet, Time course of early motor and neuropathological anomalies in a knock-in mouse model of Huntington's disease with 140 CAG repeats. *J. Comp. Neurol.* **465**, 11–26 (2003).
41. P. Zanotti-Fregonara, K. Chen, J. S. Liow, M. Fujita, R. B. Innis, Image-derived input function for brain PET studies: Many challenges and few opportunities. *J. Cereb. Blood Flow Metab.* **31**, 1986–1998 (2011).
42. D. Bertoglio, J. Verhaeghe, L. Wyffels, A. Miranda, S. Stroobants, L. Mrzljak, C. Dominguez, M. Skinbjerg, J. Bard, L. Liu, I. Munoz-Sanjuan, S. Staelens, Synaptic vesicle glycoprotein 2A is affected in the CNS of Huntington's disease mice and post-mortem human HD brain. *J. Nucl. Med.* (2021). AQ8
43. D. Bertoglio, J. Verhaeghe, S. Korat, A. Miranda, K. Cybulska, L. Wyffels, S. Stroobants, L. Mrzljak, C. Dominguez, M. Skinbjerg, L. Liu, I. Munoz-Sanjuan, S. Staelens, Elevated type 1 metabotropic glutamate receptor availability in a mouse model of Huntington's disease: A longitudinal PET study. *Mol. Neurobiol.* **57**, 2038–2047 (2020).
44. D. Bertoglio, J. Verhaeghe, A. Miranda, I. Kertesz, K. Cybulska, S. Korat, L. Wyffels, S. Stroobants, L. Mrzljak, C. Dominguez, L. Liu, M. Skinbjerg, I. Munoz-Sanjuan, S. Staelens, Validation and noninvasive kinetic modeling of [^{11}C]UCB-J PET imaging in mice. *J. Cereb. Blood Flow Metab.* **40**, 1351–1362 (2020).
45. D. Bertoglio, L. Kosten, J. Verhaeghe, D. Thomae, L. Wyffels, S. Stroobants, J. Wityak, C. Dominguez, L. Mrzljak, S. Staelens, Longitudinal characterization of mGluR5 using ^{11}C-ABP688 PET imaging in the Q175 mouse model of Huntington disease. *J. Nucl. Med.* **59**, 1722–1727 (2018).
46. A. Miranda, S. Staelens, S. Stroobants, J. Verhaeghe, Motion dependent and spatially variant resolution modeling for PET rigid motion correction. *IEEE Trans. Med. Imaging* **39**, 2518–2530 (2020).
47. G. A. Johnson, A. Badea, J. Brandenburg, G. Cofer, B. Fubara, S. Liu, J. Nissanov, Waxholm space: An image-based reference for coordinating mouse brain research. *Neuroimage* **53**, 365–372 (2010).
48. R. N. Gunn, A. A. Lammertsma, S. P. Hume, V. J. Cunningham, Parametric imaging of ligand-receptor binding in PET using a simplified reference region model. *Neuroimage* **6**, 279–287 (1997).
49. Y. Wu, R. E. Carson, Noise reduction in the simplified reference tissue model for neuroreceptor functional Imaging. *J. Cereb. Blood Flow Metab.* **22**, 1440–1452 (2002).
50. Z. Bayram-Weston, L. Jones, S. B. Dunnett, S. P. Brooks, Comparison of mHTT antibodies in Huntington's disease mouse models reveal specific binding profiles and steady-state ubiquitin levels with disease development. *PLOS ONE* **11**, e0155834 (2016).
51. M. Minderer, W. Liu, L. T. Sumanovski, S. Kugler, F. Helmchen, D. J. Margolis, Chronic imaging of cortical sensory map dynamics using a genetically encoded calcium indicator. *J. Physiol.* **590**, 99–107 (2012).
52. C. Halldin, S. Stone-Elander, L. Farde, E. Ehrin, K. J. Fasth, B. Langstrom, G. Sedvall, Preparation of 11C-labelled SCH 23390 for the in vivo study of dopamine D-1 receptors using positron emission tomography. *Int. J. Rad. Appl. Instrum. A* **37**, 1039–1043 (1986).
53. E. Ehrin, L. Farde, T. de Paulis, L. Eriksson, T. Greitz, P. Johnstrom, J. E. Litton, J. L. Nilsson, G. Sedvall, S. Stone-Elander, S.-O. Ögren, Preparation of 11C-labelled Raclopride, a new potent dopamine receptor antagonist: Preliminary PET studies of cerebral dopamine receptors in the monkey. *Int. J. Appl. Radiat. Isot.* **36**, 269–273 (1985).
54. G. Paxinos, K. Franklin, *The Mouse Brain in Stereotaxic Coordinates* (Academic Press, ed. 2, 2003), 350 pp.

Acknowledgments: We thank P. Joye, C. Berghmans, E. Van der Hallen, R. Raeymakers, S. Incardona, and A. Van Eetveldt of the Molecular Imaging Center Antwerp (MICA) and S. Jahn, N. Hoeschen, A. Kakoulidou, I. Cardaun, A. Cornelius, C. Schmidt, and T. Schwagarus at Evotec Hamburg for their important and valuable technical support; E. Galstian, M. Bader, and B. Lager for project and animal management support and administration; and S. Noble for help with proofreading the manuscript. **Funding:** D.B. is supported by a postdoctoral fellowship from the Research Foundation Flanders (FWO, 1229721N). Antwerp University, Belgium supported the work through a partial assistant professor position to J.V. and a full professor position to S. Staelens. D.B., A.V.d.L., J.V., and S. Staelens are members of the μNeuro Research Centre of Excellence at the University of Antwerp. Timelines of Figs. 2 to 5 and figs. S3 and S10 were generated using BioRender. **Author contributions:** Conception and design of the studies: D.B., J.B., L.L., M.H., A.G., C.D., J.V., S. Staelens, and I.M.-S. In vitro assays and studies: D.B., M.H., F.P., F.H., and S. Schaertl. Chemistry design of ligands and synthetic routes: C.J.B., P.D.J., M.E.P., and M.R.M. Injection ZFP for studies: A.G. and B.H. MRI: D.B., T.V., and A.V.d.L. Synthesis of radioligands: S.D.L. In vivo PET studies: D.B., A.M., F.Z., J.V., and S. Staelens. Postmortem studies: D.B., M.H., and F.Z. Supervised the experiments: D.B., J.B., L.L., M.H., A.G., L.M., V.K., Y.W., D.M.M., M.S., J.V., C.D., S. Staelens, and I.M.-S. Interpretation of the results: D.B., J.B., M.H., L.L., A.G., L.M., V.K., Y.W., D.M.M., M.S., J.V., C.D., S. Staelens, and I.M.-S. Prepared final figures: D.B. Writing—original draft: D.B., J.B., M.H., A.G., and I.M.-S. **Competing interests:** This work was supported by the nonprofit CHDI Foundation Inc. J.B., L.L., L.M., V.K., Y.W., D.M.M., M.S., C.D., and I.M.-S. are employed by CHDI Management Inc. as advisors to CHDI Foundation Inc. and declare no competing interests. CHDI Foundation Inc. is a nonprofit biomedical research organization exclusively dedicated to developing therapeutics that substantially improve the lives of those affected by HD, and conducts research in a number of different ways. The following granted patent is related to this work: Probes for Imaging Huntingtin Proteins, International Publication Number WO 2016/033445 Al (published on 3 March 2016 with filing number #PCT/US20 15/047407). **Data and materials availability:** All data associated with this study are present in the paper or the Supplementary Materials. Any request for material reported in this study will be available through a material transfer agreement (MTA) between requestor and CHDI Foundation Inc.

Submitted 13 September 2021
Resubmitted 20 September 2021
Accepted 15 December 2021
Published 2 February 2022
10.1126/scitranslmed.abm3682

Abstract

One-sentence summary: A small molecule that quantifies the causative agent of Huntington's disease can be used to assess the efficacy of therapeutic interventions.

Editor's Summary:
Revealing mHTT in real-time

Huntington's disease (HD) is caused by mutations in the gene encoding for the protein huntingtin (HTT), leading to accumulation of toxic mutant HTT (mHTT) aggregates. Development of therapies aiming to reduce mHTT is hindered by the lack of imaging methods to visualize mHTT in the living brain. Here, Bertoglio *et al.* developed a positron emission tomography (PET) imaging radioligand that could be used to measure mHTT aggregates in the brain. This probe allowed noninvasive quantification of brain mHTT in a rodent model of HD during disease development and in response to therapeutic intervention, suggesting that PET imaging using this radioligand could be used for improving diagnosis and for measuring the effects of potential therapies.

MS no: RAabm3682/KP/MEDICINE